Rydberg Composites

Andrew L. Hunter, Matthew T. Eiles, Alexander Eisfeld, and Jan M. Rost
Max Planck Institute for the Physics of Complex Systems, 38 Nöthnitzer Strasse, 01187 Dresden, Germany

(Received 3 September 2019; accepted 24 June 2020; published 26 August 2020)

We introduce the *Rydberg composite*, a new class of Rydberg matter where a single Rydberg atom is interfaced with a dense environment of neutral ground state atoms. The properties of the composite depend on both the Rydberg excitation, which provides the gross energetic and spatial scales, and the distribution of ground state atoms within the volume of the Rydberg wave function, which sculpt the electronic states. The latter range from the "trilobites," for small numbers of scatterers, to delocalized and chaotic eigenstates, for disordered scatterer arrays, culminating in the dense scatterer limit in symmetry-dominated wave functions which promise good control in future experiments. We discuss one-, two-, and three-dimensional arrangements of scatterers using different theoretical methods, enabling us to obtain scaling behavior for the regular spectrum and measures of chaos and delocalization in the disordered regime. We also show that analogous quantum dot composites can elucidate in particular the dense scatterer limit. Thus, we obtain a systematic description of the composite states. The two-dimensional monolayer composite possesses the richest spectrum with an intricate band structure in the limit of homogeneous scatterers, experimentally accessible with pancake-shaped condensates.

DOI: 10.1103/PhysRevX.10.031046

Subject Areas: Atomic and Molecular Physics, Nonlinear Dynamics, Quantum Physics

I. INTRODUCTION

Ultralong-range molecules composed of a Rydberg atom and a ground state atom, colloquially known as trilobites, were proposed in 2000 [1]. Soon thereafter theoretical explorations regarding the possibility of polyatomic molecules involving several ground state atoms followed [2,3]. The experimental verification of ultralong-range Rydberg dimers in 2009 [4] also confirmed accidentally the existence of trimers [5]. Since then, interest in Rydberg excitations beyond isolated atoms has rapidly branched out into quite diverse scenarios. These include the replacement of the ground state atom in the original trilobite dimer by larger and more complex systems, e.g., one or more polar molecules [6–9], the (re)discovery of Rydberg excitations in solid-state systems [10], and a large variety of excitonic Rydberg dynamics in the gas phase [11–13], just to name a few. For the increasingly dense gases now achievable in experiments, one can elegantly describe this system as a Rydberg excitation dressed by ground state atoms from the gas. In fact, recent experiments exhibit spectral features corresponding to polyatomic molecules containing up to five ground state atoms [14–16], and mean-field shifts in the spectrum reveal this polaronic behavior involving the coupling of many hundreds of atoms to the Rydberg electron [17]. One may wonder how many ground state "scatterer" atoms within the volume occupied by the Rydberg wave function can a trilobite molecule tolerate. A recent study found that trilobites actually thrive in a dense gas, which is counterintuitive at first glance [18]. What we lack is a systematic approach which connects the trilobite regime with a few scatterers to the regime of very dense scatterers, although the phenomena just described suggest that Rydberg excitations immersed in dense and structured media might have very interesting properties. The present investigation opens a new venue for *Rydberg composite* systems along this way, which involve many thousands of atoms in a structured environment coupled to a single Rydberg atom. These composites can be formed by exciting a Rydberg atom within a one-, two-, or three-dimensional optical lattice such that the electronic wave function envelops many atoms on the surrounding sites, but can also be created in other settings involving randomly positioned scatterers within a geometrically confined volume. We present a systematic and detailed investigation of this Rydberg composite and provide its properties as a function of principal quantum number ν, lattice constant d, and fill factor F of lattice sites.

With the Rydberg composite we change the perspective from the molecular one—using chemical approaches to characterize polyatomic trilobites via Born-Oppenheimer

potential surfaces, rovibrational couplings, etc., [2,19]—to a condensed matter one, emphasizing generic scaling principles, gross structure, and properties associated with the high density of states obtained here. This allows us to approach systematically dense atomic environments. Indeed, we will see that toward the limit of homogeneous filling a bandlike structure in the spectrum emerges. Moreover, the unique property of a Rydberg electron bound to an isolated atom with a singular point of infinite density of states (DOS) at the ionization threshold $\lim_{\nu\to\infty} E_\nu \equiv -1/(2\nu^2) = 0$ and full degeneracy makes such a Rydberg composite an interesting object to study, as the distribution of scatterers can break the degeneracy in a controlled, yet flexible, way. We identify nontrivial scaling properties as a function of ν. They allow us to connect the situation at finite ν with threshold $\nu \to \infty$. Finally, the composite's key properties are derived analytically in the homogeneous limit, while random matrix theory is used for the irregular part of the spectrum.

We also explain how a planar environment breaks the symmetry of the Rydberg composite and leads to much richer spectral structures as compared to a wirelike (one-dimensional) or crystal-like (three-dimensional) atomic environment. Hence, we put emphasis on a planar sheet of atoms arranged in a lattice containing a Rydberg excitation as an exemplary Rydberg composite whose experimental realization is facilitated by the routine creation of two-dimensional optical lattices [20] and, increasingly, the rapid progress in optical tweezer arrays [21–24]. Several of the Rydberg composite properties we study are observable in a 2D system without a regular lattice arrangement, and could be studied in sufficiently dense pancake-shaped condensates [25–28]. Moreover, we briefly discuss how quantum dots can give rise to similar composite structures. They further elucidate the dense scatterer limit, offer additional possibilities to create a composite experimentally, and underline the generality of the excitation composite idea beyond Rydberg composites.

More generally, excitation composites as introduced here describe how the high degeneracy of an underlying excitation (zeroth-order Hamiltonian) can be lifted in a controlled way. The "generic" situation of sufficiently many scatterers to remove all degeneracies exhibits chaotic level dynamics. It can be smoothly tuned to the few-scatterer limit where less degenerate polyatomic electronic symmetries replace the highly degenerate and symmetric underlying excitation spectrum. In the opposite limit of very many scatterers, the latter lose their individual role. Rather, the symmetry of their geometric support becomes dominant. If it is planar, it turns the degenerate spectrum of the Rydberg excitation into well-structured energy bands, which is a manifestation of novel correlation effects.

This paper is structured as follows. Section II provides the theoretical background. In Sec. II A, we introduce a generic Hamiltonian for composites which can describe a broad class of systems consisting of an excited object coupled to localized scatterers. Section II B specifies this Hamiltonian for our Rydberg composite in D dimensions. Section II C details the scaling properties of the Rydberg composite in one, two, and three dimensions. In Sec. III, we introduce the phenomenology of the composite in the three different lattice geometries, investigating both the DOS (Sec. III A) and exemplary wave functions (Sec. III B). In Sec. IV, we focus on the homogeneous density regime of dense scatterers where the system can be studied analytically to obtain a clear intuitive picture of the system, its band structure, and the resulting scaling laws. Section V investigates the inhomogeneous regime, using statistical measures derived from random matrix theory to understand the interplay of symmetry and chaos induced spectral features. Section VI discusses potential experimental realizations, and Sec. VII concludes with further perspectives and implications. Striving for a text which is as far as possible self-contained, we occasionally provide formulas available in standard references. Throughout we adopt atomic units.

II. THEORETICAL DESCRIPTION

A. Generic Hamiltonian

We begin with a generic description of our system, which is composed of an electron with position $\mathbf{r}$ and momentum $\mathbf{p}$ in the presence of a central potential $V(r)$ and a collection of pointlike scattering objects with positions following a distribution $\rho(\mathbf{x})$. This scatterer arrangement can correspond to either a structured geometry or a disordered environment, i.e., that found naturally in an optical lattice or in an ultracold gas, respectively. Although the electron wave function is fully three dimensional, the dimensionality of the scatterer geometry can be lower, for example, as in a one-dimensional chain or a two-dimensional random gas. The scatterers interact with the electron via the potential $U(\mathbf{x},\mathbf{r})$, which destroys the spherical symmetry of the central potential $V(r)$ and, in general, makes the system classically chaotic.

We assume a frozen-gas scenario, consistent with the ultracold temperatures of such a system, and neglect the motion of the scatterers. The electronic Hamiltonian is therefore

$$H = \frac{\mathbf{p}^2}{2m} + V(r) + \int \rho(\mathbf{x}) U(\mathbf{x},\mathbf{r}) d^3x. \tag{1}$$

This generic Hamiltonian has been studied in several contexts over the past decades, with examples ranging from two-dimensional quantum dots [29,30], quantum billiards [31], Coulomb systems [32,33], perturbed harmonic oscillators [34], and Bose-Einstein condensates (BEC) in a dimple potential [35], to name just a few. The electronic wave function for vanishing U separates in spherical

coordinates: $\Phi(\mathbf{r}) = \langle \mathbf{r}|\nu lm\rangle = u_{\nu l}(r)/r\, Y_{lm}(\theta,\phi)$, where $Y_{lm}(\theta,\phi)$ is a spherical harmonic. Therefore, mutual eigenstates of the angular momentum operator and the Hamiltonian satisfy $\mathbf{L}^2|\nu lm\rangle = l(l+1)|\nu lm\rangle$, $L_z|\nu lm\rangle = m|\nu lm\rangle$, and $H|\nu lm\rangle = E_{\nu l}|\nu lm\rangle$. Any central potential possesses azimuthal symmetry and hence has $2l+1$ degenerate states for a given ν and l. In the next section, we consider the Coloumb potential, $V(r) = -1/r$, which has an additional symmetry: it conserves the Runge-Lenz vector $\mathbf{A} = \mathbf{p}\times\mathbf{L} - \mathbf{r}/r$, leading to a particularly large degenerate Hilbert space in each manifold ν. Scatterers will lift this degeneracy. Special scatterer geometries, however, may be able to restore this degeneracy in the Rydberg composite.

B. Implementation for the Rydberg composite

The Rydberg atom is a major workhorse of modern atomic physics; here, when embedded in an ultracold medium of neutral atoms, it provides an ideal physical realization of the Hamiltonian [Eq. (1)]. For an alkali atom, typically used in an ultracold context, this means that $V(r)$ is a Coulomb potential for r larger than a few atomic units. The deviation at small r, typically set by an empirical model potential, includes the interactions with the other atomic electrons. This leads to energies $E_{\nu l}$ that are nondegenerate for the different l values of a given principal quantum number ν. However, as l increases, the wave function's overlap with this short-range region decays rapidly and $E_{\nu l} \to -(1/2\nu^2)$, degenerate in l as for hydrogen. Typically only the states with the three or four lowest l values deviate appreciably from the hydrogenic Rydberg spectrum. The overwhelming majority of states behave as in hydrogen, and therefore for simplicity we consider a hydrogenic spectrum here. For the interaction between the surrounding ultracold atoms—the localized scatterers—and the electron, we use the Fermi pseudopotential [1,36],

$$U(\mathbf{x},\mathbf{r}) = 2\pi a_s(k_\mathbf{x})\delta^3(\mathbf{x}-\mathbf{r}) = 2\pi a_s(k_\mathbf{x})|\mathbf{x}\rangle\langle\mathbf{x}|, \quad (2)$$

which is straightforward to implement. The strength of each scatterer's contribution is given by the energy-dependent s-wave electron-atom scattering length $a_s[k_\mathbf{x}]$ [37]. This simple contact potential is a reasonable approximation since a neutral atom in its ground state is a highly localized and isotropic perturbation when compared to the Coulomb potential and Rydberg wavelength. It therefore imparts only an s-wave phase shift onto the Rydberg wave function via elastic scattering, as characterized by the scattering length. The energy dependence of this process is set by the semiclassical electron momentum, $k_x^2 = -(1/\nu^2) + (2/|\mathbf{x}|)$.

We neglect contributions from higher partial waves which could be included in Eq. (2) via the generalization introduced in Ref. [38]. In the alkali atoms the p-wave energy shift becomes large relative to the s-wave shift only when the electron's kinetic energy is resonant with the p-wave shape resonance in the electron-atom system. In rubidium, for example, the momentum k_x reveals that this resonance condition is met when the internuclear separation is approximately $1000a_0$. For the large principal quantum numbers we consider here, this affects only a very small number of the participating atoms and therefore has negligible effect. Atoms with shape resonances at higher scattering energies (e.g., Li or Na) or those without shape resonances (e.g., Sr) have even smaller contributions from this term [39].

For the Rydberg composite, Eq. (1) reads

$$H = -\sum_{\nu lm}\frac{|\nu lm\rangle\langle\nu lm|}{2\nu^2} + 2\pi\int d^3x\rho(\mathbf{x})a_s(k_x)|\mathbf{x}\rangle\langle\mathbf{x}|. \quad (3a)$$

The eigenstates,

$$|\Psi_i\rangle = \sum_{\nu lm} c^{(i)}_{\nu lm}|\nu lm\rangle, \quad (3b)$$

and eigenvalues E_i of the Hamiltonian (3a) are parametrized by the distribution $\rho(\mathbf{x})$ of scatterer locations. We are interested in scatterers in D-dimensional lattice configurations, and hence choose

$$\rho(\mathbf{x}) = \sum_{i=1}^{N_D}\delta^3(\mathbf{x}-\mathbf{R}_i), \quad (3c)$$

where the scatterer positions $\mathbf{R}_i = d\sum_{j=1}^{D} n_{ij}\hat{e}_j$ are located at lattice positions described by unit vectors $\hat{e}_j$, the lattice spacing d, and a set of $D\times N_D$ integers n_{ij}. Here, $D = 1,2,3$ refers to a $1D$ chain, a $2D$ and a $3D$ lattice, respectively. By excluding some values i we can implement partial filling, defined by the fill factor F. Equation (3a) relies on two more approximations: the scattering length is energy independent and the basis is truncated to only a single ν manifold. We demonstrate in Sec. IV that these approximations are increasingly accurate at high ν. They have only minor quantitative effects on the main conclusions of our study but allow us to obtain analytical formulas and clear scaling behavior. Note that the singular three-dimensional δ-function potential leads to diverging energy shifts as the number of ν manifolds included in the basis increases, making quantitatively accurate convergence challenging unless alternative Green's function techniques are used [5,40]. Reference [40] has demonstrated that the Green's function results for the s-wave dominated states investigated here are quantitatively best approximated by the results obtained using a single ν manifold in the diagonalization. A Green's function approach for arbitrary number of scatterers has yet to be implemented. Since we consider only a single ν manifold, in the following discussion we set $-(1/2\nu^2)$ to zero.

Hence, the spectrum of Eq. (3a) with the distribution from Eq. (3c) is obtained by diagonalizing the matrix

$$V_{lm,l'm'} = 2\pi a_s \sum_{i=1}^{N_D} \langle \nu lm|\mathbf{R}_i\rangle\langle \mathbf{R}_i|\nu l'm'\rangle. \quad (4)$$

In this description of the Rydberg composite we have neglected spin degrees of freedom, i.e., the fine and hyperfine structure of the Rydberg and ground state atoms. These effects are important at a quantitative level [41–43], but are not important at the qualitative level considered here, particularly since the fine structure of the high angular momentum states which dominate the composite's physics is extremely small. As with the contributions from $l \neq 0$ partial waves, spin effects can also be reduced by using certain atomic species without hyperfine structure or by appropriate spin polarization in the initial gas. Recently, progress has been made in including some spin degrees of freedom into the description of Rydberg impurities in dense bosonic gases [44].

C. Scatterer induced properties in D-dimensional lattices

The properties of the Rydberg composite, defined by the Hamiltonian in Eq. (3a), depend on the properties of both the unperturbed electronic states $|\nu lm\rangle$ and the scatterer distribution $\rho(\mathbf{x})$. The Rydberg atom's size, density of states, and wavelength are determined by its principal quantum number ν, while $\rho(\mathbf{x})$ depends on the desired lattice geometry, lattice spacing, and filling realization. In this section we delineate the important quantities for one-, two-, and three-dimensional scatterer configurations.

Although the spatial scale of the lattice can greatly exceed the size of the Rydberg wave function, not all scatterers perturb the Rydberg states since the electron-atom interaction is highly localized. Its strength, within the Fermi approximation [Eq. (2)], is determined by the electronic density directly at each scatterer's position. The Rydberg volume is finite with a radius $r_0(l) \approx a_l \nu^2$, where a_l decreases from $a_l \approx 2$ for the $l = 0$ state to $a_l \approx 1$ for the $l = \nu - 1$ states. Numerically, we only consider scatterers inside a radius $r = a_\nu = a\nu^2$ with $a > 2$, as scatterers beyond the boundary of this volume contribute negligible energy shift since all wave function amplitudes are exponentially small there. The number N_D of relevant scatterers is then determined by the volume V_D of the intersection of the Rydberg wave function and the lattice. In this way, even for an infinite lattice, we can truncate its effect to that from the N_D individual scattering potentials in Eq. (3a).

A 1D array of scatterers is depicted in Fig. 1(a). The relevant 1D volume is $V_1 = 2a\nu^2$, and $N_1 = 2a\nu^2/d$ scatterers lie within this volume. The corresponding volume for a 2D lattice is the area of the projection of the Rydberg volume into the plane, $V_2 = \pi a^2\nu^4$, and hence the number of scatterers is $N_2 = (\pi a^2\nu^4)/d^2$. In 3D we consider a cubic lattice of scatterers, and so the relevant volume is the entire Rydberg volume, $V_3 = \frac{4}{3}\pi a^3\nu^6$, containing $N_3 = 4\pi a^3\nu^6/(3d^2)$ scatterers. The values for N_D given here are valid only in the $N_D \gg 1$ limit, where edge effects due to the incommensurate spherical and Cartesian geometries are negligible.

The scatterer configuration also influences how many of the degenerate states of the Rydberg manifold are shifted. As a general rule, each scatterer splits away one state from the degenerate manifold until the geometry-induced limit B_D is reached (see the Appendix F). In a generic 3D scatterer array this limit is given by all states of the manifold, $B_3 = \nu^2$, while $B_D < \nu^2$ in 1D and 2D. To determine B_D for each case we select a convenient quantization axis and identify the Rydberg states not affected by the δ-function potential [Eq. (2)].

In 1D, we set the quantization axis parallel to the linear lattice of scatterers. When $\mathbf{r} \to R\hat{z}$, most angular

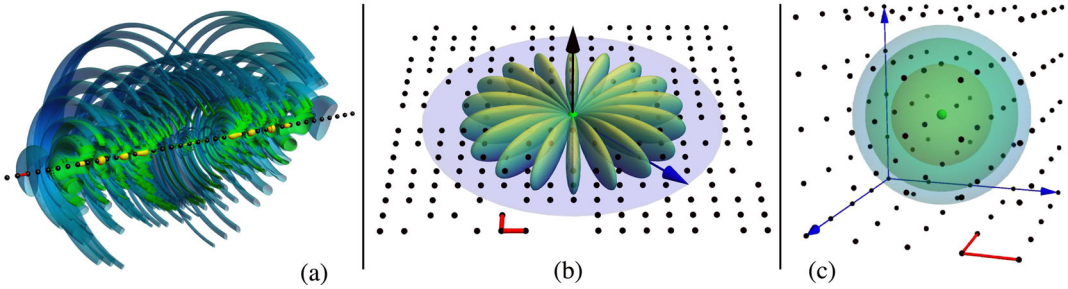

FIG. 1. Schematics of the three scenarios we consider: (a) a linear lattice (1D), (b) a monolayer (2D), and (c) a cubic lattice (3D) with the Rydberg ion in the center, respectively. In each panel the black spheres represent scatterers sitting on lattice sites and the red lines give the lattice spacing d. The missing scatterers in (b) represent a situation with incomplete filling. The volume of scatterers situated within the Rydberg wave function is represented by the blue circle in (b) and by the sphere in (c). The exemplary densities shown give different representations of the composite's electronic wave function in these three scenarios. In (a) the strongly perturbed wave function is shown with three surfaces of constant density, revealing the exotic nature of these wave functions. The full 3D contour is cut away in front to reveal the interior structure. Figure 3 provides details of the plot parameters. Panel (b) shows a contour of the angular dependence of a typical circular state, which plays a crucial role in the 2D composite's properties (see Sec. IV). Panel (c) shows an illustration of the Rydberg atom, illustrating that the spatially varying probability cloud spans many lattice sites of the 3D lattice.

wave functions vanish on the quantization axis since $Y_{lm}(\theta=0,\phi)=\sqrt{(2l+1)/4\pi}\delta_{m0}$. Only $m=0$ states experience a shift, and hence $B_1=\nu$ is the total number of $m=0$ states.

For the 2D case we set the quantization axis normal to the plane and evaluate the angular wave functions at $\theta=\pi/2$. The Legendre polynomials with argument $\cos(\pi/2)=0$ are

$$P_l^m(0)=\begin{cases}(-1)^{(l+m)/2}\frac{(l+m-1)!!}{(l-m)!!} & l+m=\text{even}\\ 0 & l+m=\text{odd.}\end{cases} \tag{5}$$

The plane is transparent to the Rydberg states possessing a node in the plane. Therefore,

$$B_2=\frac{\nu(\nu+1)}{2}. \tag{6}$$

With the help of B_D we can define a third quantity, the characteristic lattice spacing d_D such that $N_D\approx B_D$ for that geometry. This spacing heralds the onset of the density shift regime where additional scatterers cannot split away new states since the ν manifold is saturated. They instead contribute linearly to a mean-field energy shift, consistent with the conclusion drawn from the original applications of Fermi's pseudopotential [45,46]: the mean-field effect of the interaction of the Rydberg electron with the scatterers is an energy shift proportional to the electron-atom scattering length and to the scatterer density. The values for this characteristic length, along with the other values V_D, N_D, and B_D, are given in Table I. From these characteristic properties we can assess the behavior and crude scaling with ν of the Rydberg composite for a given scatterer geometry. Note that d_D is linear in ν for $D\leq 2$, but follows $\nu^{4/3}$ for the 3D case.

This analysis suggests that for sufficiently large number of scatterers N_D we will obtain B_D nonzero eigenvalues upon diagonalizing H within a ν manifold, and as a function of decreasing d these eigenvalues will grow (on average) linearly with the number of scatterers. In order to remove this asymptotic shift we normalize the total energy shift by N_D. Furthermore, we measure energies in units of $(2\pi|a_s|)^{-1}$ in order to remove the numerical prefactor from the potential matrix [Eq. (4)], and hence eliminate the material-dependent value of the scattering length from our calculated energy shifts. Finally, since N_D depends on the arbitrary (provided it is sufficiently large) choice of a, we scale the energy shifts of the D-dimensional lattice by a^D to eliminate this scale choice. Of course, in the limit $a\to\infty$, this choice removes all dependence on a and we can report scaled energies $\tilde{E}$ defined in terms of the unscaled eigenvalues E via

$$\tilde{E}=\left(\frac{d}{\nu^2}\right)^D\frac{E}{2\pi|a_s|\tilde{V}_D}, \tag{7}$$

where $\tilde{V}_D$ is the volume of a D-dimensional sphere with unity radius.

D. Implementation for the spherical quantum dot composite

Equation (1) has been written in a generic form, and it is both theoretically instructive and experimentally relevant to consider other systems with high degeneracy to form the composite, as they open up new experimental possibilities and provide useful theoretical comparisons. One such system is an isotropic three-dimensional harmonic oscillator. This potential is clearly of foundational importance in quantum mechanics, but it also has physical relevance as it can be a good approximation for many other types of potentials, in particular for a spherical quantum dot (SQD). Since it is one of the few potentials which, like the Coulomb potential, has an infinite number of states, high degeneracy, and has analytically known solutions in spherical coordinates, it is an ideal system to study further aspects of the composite's properties.

As for the Coulomb potential, the wave functions $\langle\mathbf{r}|\mu lm\rangle$ of the harmonic oscillator potential $V(r)=\frac{1}{2}m\omega^2r^2$ can be written as a product of the spherical harmonic $Y_{lm}(\hat{r})$ times a radial function. It is given by

TABLE I. Scaling properties for the Rydberg composite (when the principal quantum number ν is used) or the SQD composite (when μ is used) in terms of the effective system radius, $a_\nu=a\nu^2$ or $a_\mu=a[(3+2\mu)/\omega]^{1/2}$. Note that $A_\mu=B_\mu=\mu+1$ when μ is an even integer, and $A_\mu=\mu+1$, $B_\mu=\mu+3$ when μ is odd. Where unspecified, the corresponding expressions for a SQD composite with principal quantum number μ are obtained by replacing $\nu\to\mu$; see Sec. II D.

Dimension (D)	1	2	3
Effective lattice volume (V_D)	$2a_\nu$	πa_ν^2	$\frac{4}{3}\pi a_\nu^3$
Number of scatterers (N_D)	$2(a_\nu/d)$	$\pi(a_\nu/d)^2$	$\frac{4}{3}\pi(a_\nu/d)^3$
Number of shifted states (B_D)	ν	$\nu(\nu+1)/2$	ν^2
	μ	$A_\mu B_\mu/4$	$(\mu+1)(\mu+2)/2$
Maximum lattice spacing (d_D) such that $N_D=B_D$	$a_\nu/(2\nu)$	$\sqrt{2\pi}(a_\nu/\nu)$	$\sqrt[3]{(4\pi)/3}(a_\nu/\nu^{2/3})$
	$a_\mu/(2\mu)$	$\sqrt{2\pi}(2a_\mu)/\mu$	$\sqrt[3]{\pi/3}(2a_\mu)/\mu^{2/3}$

$$u_{\mu l}^{\mathrm{HO}}(r) = \mathcal{N}_{\mu l} r^{l+1} e^{-\omega r^2/2} L_{(\mu-l)/2}^{l+1/2}(\omega r^2), \tag{8}$$

with the normalization constant

$$\mathcal{N}_{\mu l} = \sqrt{\sqrt{\frac{\omega^3}{4\pi}} \frac{2^{\mu/2-3l/2+3}(\frac{\mu-l}{2})!(\omega/2)^l}{(\mu+l+1)!!}}. \tag{9}$$

The SQD's principal quantum number μ is analogous to the Rydberg principal quantum number ν. It defines the energy via

$$E_\mu = \omega(\mu + 3/2). \tag{10}$$

All eigenstates with $|m| \leq l$, $0 \leq l \leq \mu$, and $n_r = (\mu - l)/2$ are degenerate, where n_r is the number of radial nodes. In total there are $\frac{1}{2}(\mu+2)(\mu+1)$ degenerate levels in a given manifold for a 3D composite, and due to the same parity selection rule for $l+m$ as in the Rydberg composite, about half of these states are shifted in the 2D composite. The size of the system—the equivalent to a_ν used in the Coulomb case—is given by $a_\mu = a[\omega^{-1}(3+2\mu)]^{1/2}$, where we choose $a > 1$ to ensure exponential decay of all wave functions within this volume. The parameters for the excitation composite are given in Table I.

III. PHENOMENOLOGY OF THE RYDBERG COMPOSITE

The spectrum of a Rydberg atom immersed in a structured neutral medium depends on both the Rydberg principal quantum number and the different realizations of the lattice. We parametrize the latter by the filling factor F, the percentage of filled lattice sites, and by the lattice spacing d. We focus first on unity filling factor so that we can introduce the essential quantities useful in characterizing the composite's properties. In Sec. V we remove this restriction and study fractional filling.

We first study the density of states. It reveals more about the global spectral properties than individual energy levels, and provides a useful guide to regions of interest to focus on in finer detail. In a second step, guided by the features seen in these DOS, we study the wave functions corresponding to various paradigmatic states. The structure present in these wave functions provides additional investigative tools to understand the spectra. Since the 2D monolayer leads to the richest structure in the dense lattice limit, we focus on that geometry.

A. Density of states

We show DOS in Fig. 2 for the lattice geometries depicted in Fig. 1. We observe that all B_D shifted eigenenergies converge to constant limits for $d \to 0$, as anticipated. Intriguingly, we find that the asymptotic value differs remarkably across the three geometries.

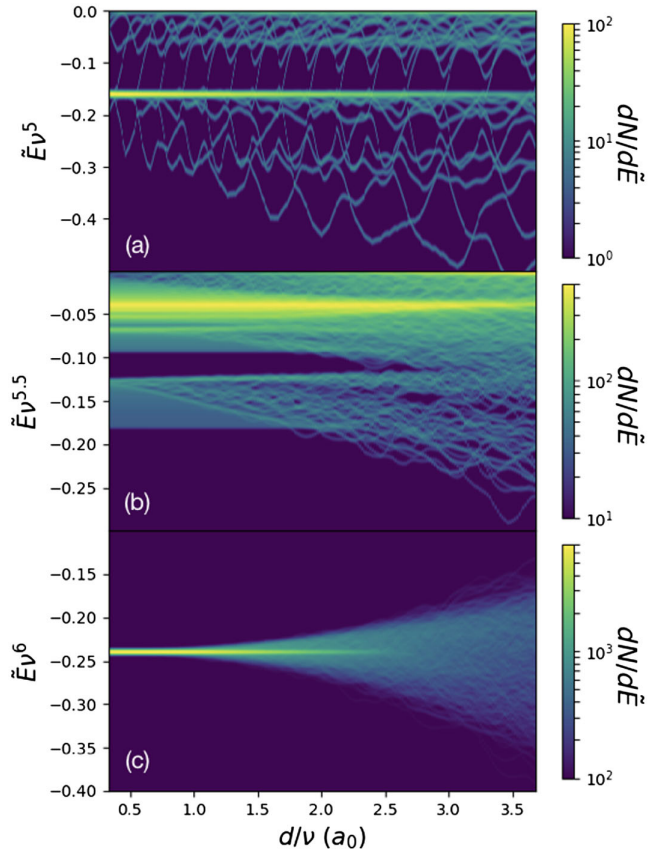

FIG. 2. Density of states $dN/d\tilde{E}$ for a $\nu = 30$ composite in 1D (a), 2D (b), and 3D (c) as a function of scaled lattice spacing d/ν.

For the 1D and 3D scatterer geometries the shifted eigenenergies become degenerate again as $N_D \to \infty$, albeit at a large overall energy shift relative to the zero-scatterer degenerate manifold. In contrast, eigenenergies in the 2D geometry remain nondegenerate even in the infinite density limit, instead developing three main features (see also the spectrum, Fig. 5): a nearly continuous and quasiuniformly spaced distribution of energy levels within a few "bands," the formation of a large "band gap" that persists even up to relatively large lattice constants, and the formation of a large peak in the DOS in the upper part of the spectrum.

As d increases the DOS becomes challenging to interpret due to the increasing number of nondegenerate energies in all three lattice geometries. In general, the spectrum diffuses. In 1D, the degenerate band is depleted as individual states split away with increasing d. This process does not occur symmetrically with respect to the degenerate band. In 3D, all states begin to split apart at approximately the same value of d and the perturbed band dissipates far more rapidly than in 1D; this process occurs symmetrically about the homogeneous energy asymptote. In 2D, the states are not degenerate in the $d \to 0$ limit. For increasing d, states higher in the energy band begin to disperse linearly in d, revealing a clear energy-dependent transition between the indistinguishable ($d \approx 0$) and distinguishable scatterer

case. In all three geometries, oscillations in the energy levels mimic the oscillatory nature of the Rydberg wave function, which is imposed quite directly onto the energy levels via the contact potential. The "spaghetti" nature of the energy levels in the large d regime reveals the presence of both real and avoided level crossings if d is taken as an adiabatic parameter. Real crossings are possible since the electronic states mirror the lattice symmetry, and therefore can be grouped according to the irreducible representations of the nuclear point group for that lattice. We have confirmed that, in the 2D lattice case, the DOS can be computed independently for each of the five irreducible representations of the C_{4v} point group, following the description of Refs. [2,19]. This is discussed in more detail in Appendix C. Finally, as d grows further, the DOS (not pictured) collapses gradually back into a highly degenerate peak at zero energy as the number of scatterers falls below B_D.

B. Wave function characteristics

We now present a representative sample of the wave functions giving rise to these DOS in 1D and 2D, which are particularly amenable to this treatment since all relevant information can be gleaned and easily visualized with three-dimensional contour plots (1D) or the $z = 0$ slice through the electron density (2D). From these wave functions we begin to see the underlying structure of the Rydberg composite and how it might lead to the emergence of the structured nondegenerate bands in 2D rather than a single, fully degenerate band in 1D and 3D. Although our focus now is descriptive, merely commenting on the appearance and classification of these wave functions, we use these observations in the following section to develop quantitatively accurate approximations which lead to a full interpretation of the Rydberg composite's properties.

1. 1D lattice wave functions

In Fig. 3 we present, for four different lattice spacings, two representative wave functions for the $\nu = 30$ 1D Rydberg composite. On the left we show the state with the largest energy shift, while on the right we choose a state slightly higher in energy than the degenerate band limit, i.e., one of the states visible in Fig. 2(a) just above the middle band. These wave functions visually forge the connection between Rydberg composites and "trilobite" molecules [2,3,19,47]. At large d, shown in the bottom row, the wave function is a mixture of many l states, leading to strong localization on scatterer positions. In scenarios such as this where scatterers are separated by distances greatly exceeding d_D, the wave function tends to localize on only a subset of the scatterers and effectively ignore the rest. In this way it maximizes the overlap between the Rydberg electron and the lattice, and ensures orthogonal wave functions. As d decreases these states eventually begin to resemble the hydrogenic basis states and localize less

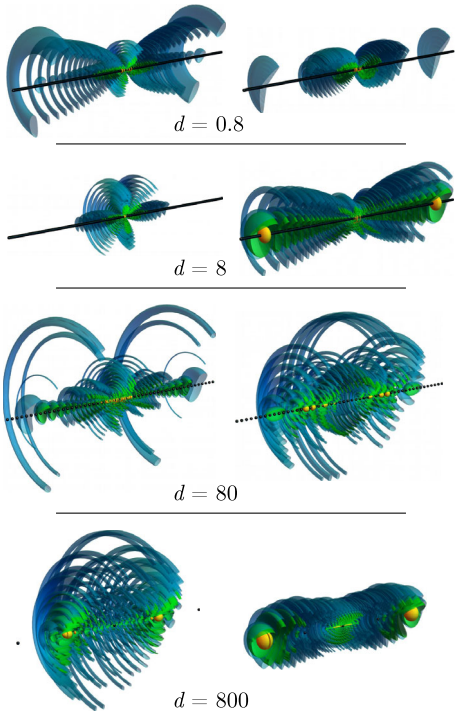

FIG. 3. Electronic densities of a 1D lattice of scatterers for $\nu = 30$ and different lattice spacings d in atomic units. The yellow, green, and blue surfaces correspond to contours at wave function densities spanning factors of 10. The full three-dimensional surfaces are cut away in front to reveal the interior structure. The left-hand column gives the density for the most deeply perturbed state, while the right-hand column gives the density just above the degenerate band.

severely on a symmetry-imposed collection of scatterers, as the Rydberg wave function increasingly cannot distinguish scatterers lying closer together than its wavelength. Unfortunately, these wave functions do not as yet reveal with any clarity why the infinite density limit of this 1D composite is again an energetically degenerate system. A key reason for this uncertainty is, in fact, their degeneracy: degenerate eigenstates obtained via a numerical diagonalization will in general be arbitrary superpositions of the linearly independent states. It is thus impossible to identify any possible good quantum numbers or selection rules from these wave functions without investigating some other observable. In principle, this could be done by applying a magnetic field to break apart the degeneracy at large scatterer density. For our present purposes we can turn instead to the 2D composite, which is fundamentally nondegenerate in this limit and may reveal through its wave functions the underlying structure of the 1D case.

2. 2D lattice wave functions

Since only the electronic density in the $z = 0$ plane contributes to the energy shifts, it suffices to examine $|\Psi(x, y, 0)|$ for the 2D composite. We first consider the

wave functions of the 2D composite with a fully filled 2D lattice and vary the lattice constant. In Fig. 4 (bottom) we show the wave functions corresponding to the first three odd-numbered eigenenergies starting from the lowest one. For large enough d the electron density obeys one of the discrete symmetries permissible by the C_{4v} point group, and partially localizes on only a subset of the available scatterers. The behavior of this localization and its effect on the energy-level structure likely warrants future study. As d shrinks further, the electron density evolves into a distinctly circular shape. By the lowest d shown ($d = 20$), these three eigenstates have seemingly converged into "circular" states. By a strict definition, a circular Rydberg state has $l = m = \nu - 1$; here we employ a broader definition meaning a state with high l and $|m|$, but with only a small difference $l - |m|$. The second and fourth eigenstates identically resemble the first and third, respectively, showing that the $\pm m$ states are equivalent and degenerate in this limit.

To confirm that these eigenstates do not arise due to some coincidence in the symmetry-adapted wave functions or fortuitous overlap with the lattice grid, we next consider a lattice with a small lattice constant $d \ll d_D$ but with varying fill factor F. At extremely low F [first column of Fig. 4 (top)], having only a few scatterers, we see that the nondegenerate eigenstates are basically independent trilobite dimers between the Rydberg core and each individual scatterer. As F increases, the number of scatterers increases rapidly and the wave function becomes rather chaotic in appearance, exhibiting no clear structure. In some instances it localizes asymmetrically about statistical fluctuations in the random scatterer distribution where small clusters form spontaneously.

As before, when the series progresses toward complete filling, the density resembles more and more a circular state, thus confirming that the appearance of such states depends more on the total density of scatterers relative to the number fluctuations caused by random fill factors than on the underlying lattice symmetry. Once fluctuations and correlations in the scatterer density are unresolved by the Rydberg wave function, any choice of random fill factor is essentially indistinguishable and the result from the $F = 1$ case is reached.

C. Role of wave function character in the 2D spectrum

Both ways of increasing the scatterer density described above lead to the following conclusion in the high-density limit: the wave functions become increasingly circular in character, implying that they become approximate eigenstates of $\hat{L}_z$. This is to be expected in the limit of a totally homogeneous lattice, where H commutes with $\hat{L}_z$ due to the cylindrical symmetry. Of greater interest is the fact that the energies of these states are also apparently sorted by the level of circularity, as states with the most circular character

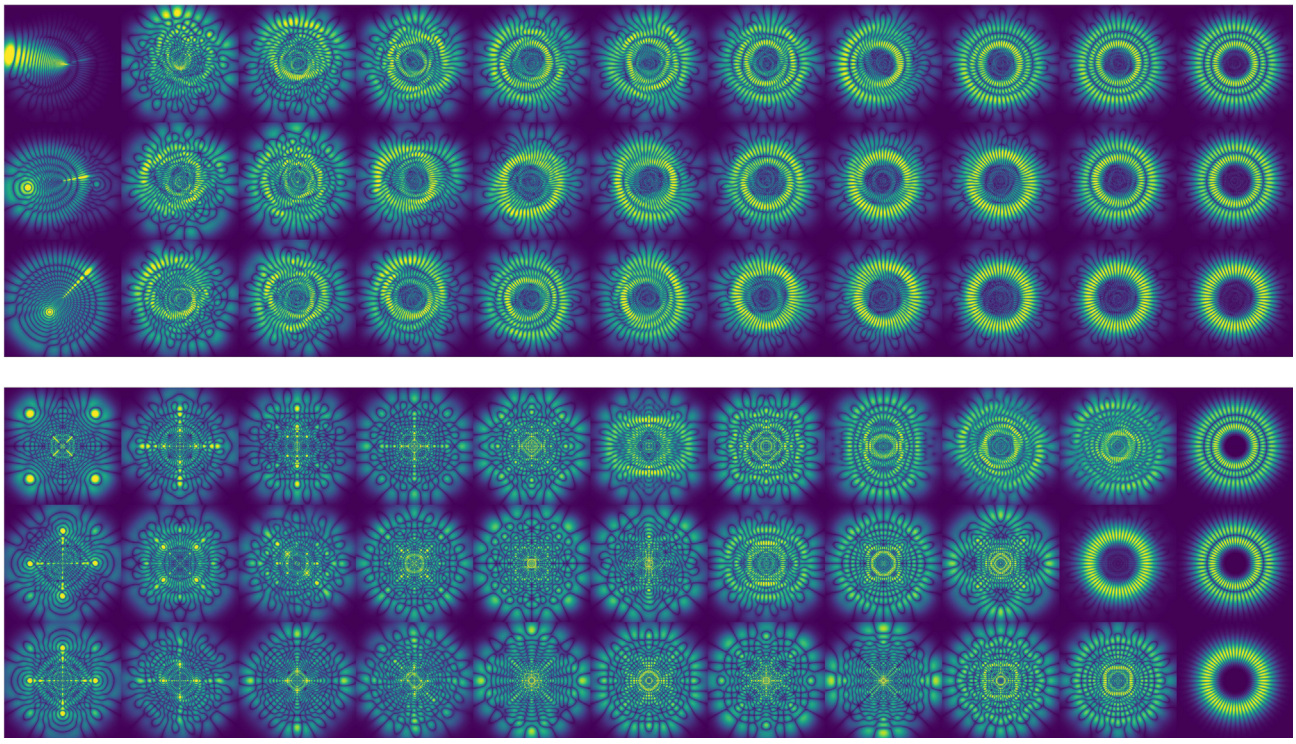

FIG. 4. The electron density $|\Psi(\mathbf{r})|^{1/2}$ of selected eigenstates of a $\nu = 30$ 2D composite. Both panels display from bottom to top the first, third, and fifth eigenstates. Top: Probability densities for a dense lattice ($d = 20$) increasing in fill factor from left to right in steps of 0.1 excluding the first panel where only five scatterers are present. Bottom: Probability densities for a full lattice with $d = \{1000, 500, 300, 200, 100, 90, 80, 70, 60, 54, 20\}$, respectively.

fall to the bottom of the energy bands. A useful diagnostic to analyze the evolution of the composite as d or F changes is to monitor the participation ratio P_{PR} of degenerate $\pm m$ manifolds in each eigenfunction Ψ_i expanded in the basis $|\nu l m\rangle$ [see Eq. (3b)]

$$P_{\mathrm{PR}} = \sum_{m=0}^{\nu-1} \left(\sum_{l=m}^{\nu-1} \frac{|c_{\nu l m}^{(i)}|^2 + |c_{\nu l -m}^{(i)}|^2}{1+\delta_{0m}} \right)^2. \tag{11}$$

This quantity ranges from 1, for a state where m is a good quantum number, to $1/\nu$, for a state mixed uniformly among m manifolds. In Fig. 5 we show the 2D composite's eigenspectrum as a function of d. Although this conveys very similar information as the DOS plot in Fig. 2, coloring the eigenstates by P_{PR} reveals additional structure in these energy levels that can be linked to the wave function. The P_{PR} distinguishes many self-similar and repeating substructures that were not evident in Fig. 2(b). Several "bands" of states with a similar functional dependence on d and pattern of P_{PR} are visible, separated by the large energy gap that was clear in the DOS as well. These bands become indistinguishable toward high energy and converge into the region of high degeneracy seen in Fig. 2. The clear transition between states with $P_{\mathrm{PR}} \approx 1$, which have m as a good quantum number, and those which are strongly mixed helps differentiate these bands even when they start to overlap. This transition is well predicted by a critical lattice spacing (d_c) defined in Sec. V and shown for the first three bands in Fig. 5 as black curves. Figure 5 shows that the trend toward circular states in the few eigenstates presented in Fig. 4 is emblematic of a more general behavior: in the $d/\nu \ll 1$ limit, H commutes with $\hat{L}_z$ and hence all wave functions have m as a good quantum number, of which the circular states are a small subset. From the wave functions in Fig. 4 we see also that the lowest states of the energy bands approximately conserve l as well, with maximal or nearly maximal values of both quantum numbers.

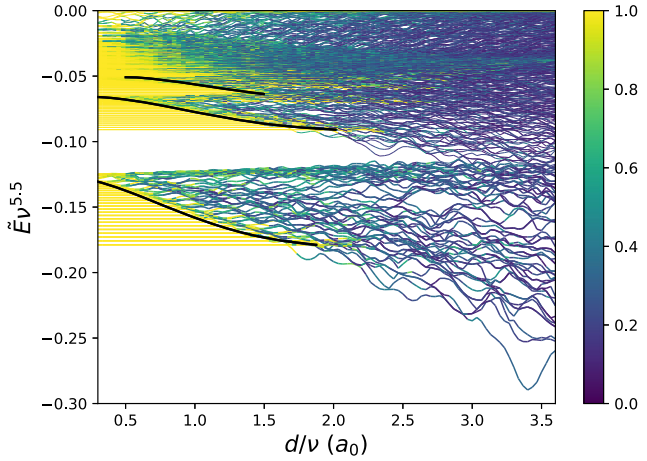

FIG. 5. Spectra for a $\nu = 30$ 2D Rydberg composite as a function of lattice spacing. The line color shows P_{PR} for each state as defined by Eq. (11). The black line marks the border between homogeneous and inhomogeneous regimes [see Eq. (34)].

We devote much of the remainder of this paper to the 2D composite, since embedding the Rydberg excitation in a planar environment constitutes a new scheme in ultracold Rydberg physics with a rich and intricate behavior. In particular, we explicate the physics underlying these (so-far phenomenological) observations: the formation of energy bands separated by a single dominant band gap and the relatively simple character of the underlying wave functions. We elucidate the link between this structure and the structure underlying the Hamiltonian matrix. The mathematical tools used for this task also enable us to understand why all states become degenerate in a homogeneous 1D or 3D environment but not in a planar one. Furthermore, these tools prove useful as a launching point for our later investigation of disorder in dilute lattices with random filling and lattices with larger d.

IV. RYDBERG COMPOSITE PROPERTIES IN THE HOMOGENEOUS DENSITY LIMIT

Our investigation of the 2D composite's spectrum starts with the observation that, below a certain lattice constant $d < d_c$, the Rydberg wave function can no longer resolve individual scatterers. The lattice then appears homogeneous, and the phenomenology of previous sections has shown that the spectrum becomes constant. In the present section, we take it as fact that this coarse graining is physically relevant and use it to approximate the discrete lattice of scatterers with a continuous plane of homogeneous density. In this way we characterize the system's properties for the $d \ll \nu$ region of Figs. 2 and 5, which is then crucial to properly situate our analysis for intermediate cases with $d > d_c$ or $F < 1$.

A. 2D monolayer: Emergence of a band structure

The replacement of the discrete lattice with a homogeneous distribution coincides mathematically with the replacement of the summation in Eq. (4) with an integral. In the scaled energy units this replacement must include also a factor V_2^{-1}, and the matrix elements become

$$\lim_{d\to 0} \tilde{V}_{lm,l'm'} = \frac{a_\nu^2 \int \Phi_{\nu lm}^*(R,\frac{\pi}{2},\varphi)\Phi_{\nu l'm'}(R,\frac{\pi}{2},\varphi)d\mathcal{A}}{V_2}, \tag{12}$$

with integration over the entire plane. Using the spherical coordinate representation of these wave functions, the integral over φ gives the standard orthogonality relation $\delta_{mm'}$. Two additional contributions to the matrix elements emerge, a radial overlap integral,

$$\mathcal{R}_{\nu l,\nu l'}^{(j)} = \int_0^\infty \frac{u_{\nu l}(R)u_{\nu l'}(R)}{R^j} dR, \tag{13}$$

and the projection of the spherical harmonics into the plane, $\mathcal{P}_{lm,l'm'} = N_{lm}P_l^m(0)N_{l'm'}P_{l'}^{m'}(0)$, where

$$N_{lm} = \sqrt{\left(l+\frac{1}{2}\right)\frac{(l-m)!}{(l+m)!}}, \tag{14}$$

and $P_l^m(\cos\theta)$ was given in Eq. (5). As expected, integration over φ imposes a block-diagonal structure in m on this matrix, since the homogeneous scatterer limit is isotropic. Equation (12) therefore yields

$$\lim_{d\to 0}\tilde{V}_{lm,l'm'} = \frac{\delta_{mm'}}{\pi\nu^4}\mathcal{P}_{lm,l'm}\mathcal{R}^{(1)}_{\nu l,\nu l'}. \tag{15}$$

Figure 6 displays the eigenvalues of this block-diagonal matrix, plotted as a function of m to emphasize the parallels with a band structure. We see that the resulting eigenvalues can be sorted into energy bands which are linear in the wings at high $|m|$ and quartic near $|m| = 0$. We label these with a band index β, thereby characterizing each eigenenergy by a (β, m) label. As β increases, the wings of upper bands begin to overlap the flat low-$|m|$ regions, and we find in this overlapping region that each band begins along the essentially continuous line $\tilde{E} = -(m/\sqrt{2\pi\nu^3})$.

To understand the formation of these bands as well as to obtain analytic results for the eigenspectrum, we study the matrix elements of each m-level block of the Hamiltonian. As one might surmise from the wave function study in the previous section, these sub-blocks appear to be diagonal dominated for moderate to high l and m. This can stem from two influences. First, the off-diagonal couplings tend to be around one order of magnitude smaller than the diagonal matrix elements. This is because, although the radial overlap integral does not have a rapid dependence on l, the $u_{\nu l-2}(R)$ wave function has a node nearly at the maximum antinode of the $u_{\nu l}(R)$ function, and hence the integrand of off-diagonal elements $\mathcal{R}^{(1)}_{\nu l,\nu l'}$ is small compared to their diagonal counterparts $\mathcal{R}^{(1)}_{\nu l,\nu l}$. An additional and more critical contribution stems from the spherical harmonic projections onto the plane, which are illustrated with surface contour plots in Fig. 7 for these circular states. Each column of this figure contains all the states within a single m block, starting with $m = \nu - 1 = l$ on the left and decreasing by 2 [because of the selection rule of Eq. (5)] with each step to the right. The orbital angular momentum l decreases by 2 with each vertical step up from its maximal value, $l = \nu - 1$, in the bottom row. Since l cannot be less than $|m|$, the size of each sub-block increases with decreasing m. There is no coupling between columns, which come from different m blocks. Clearly, the states within each column have dramatically different overlap with the $z = 0$ plane since each drop in l pushes an additional lobe out of the plane. These contribute nothing to the total energy shift and are essentially "wasted" probability. In contrast, along the diagonals marked by red the wave functions are nearly identical. Moving up the diagonal swaps an angular lobe into a (not pictured) radial

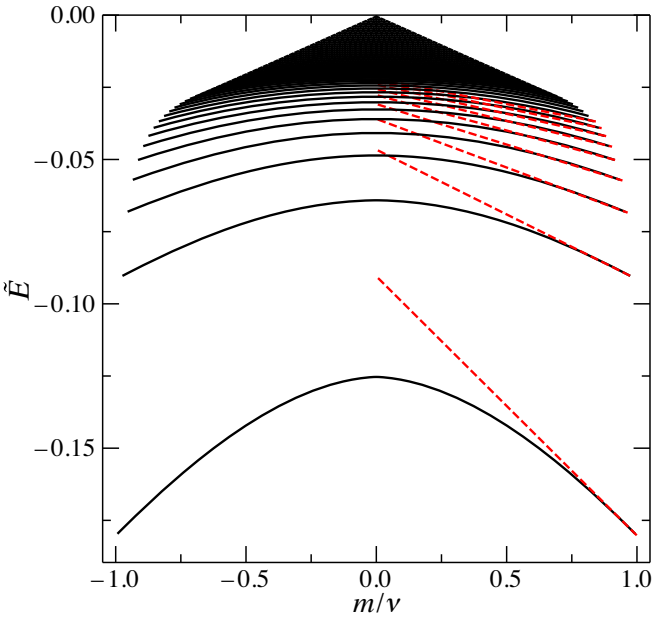

FIG. 6. The 2D Rydberg composite's spectrum displayed as a dispersion relation, emphasizing the formation of energy bands. The black curves show $\tilde{E}(m/\nu)$ for $\nu = 100$. The dashed red lines are the asymptotic linearization of Eq. (17).

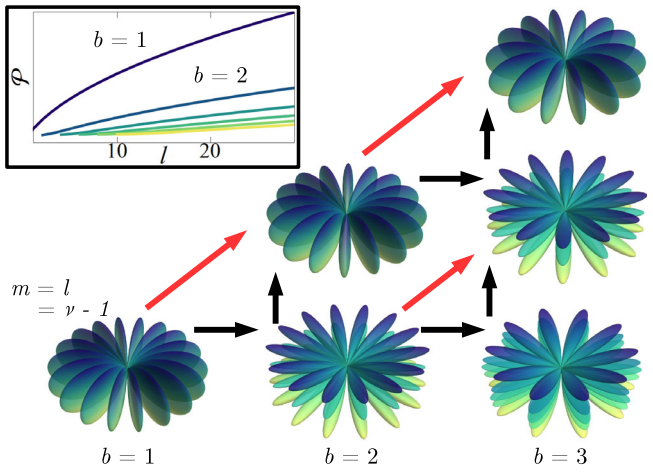

FIG. 7. Dependence of the band structure of a 2D Rydberg composite on the projection of $Y_{lm}(\theta,\varphi)$ into the plane. Shown are a few spherical harmonics, starting in the bottom left-hand corner with the maximally circular state. Horizontal black (vertical black) arrows represent a decrease in m (l). States in the same column therefore are from the same block diagonal. Red diagonal arrows represent increases in $k = \nu - l$, starting from $k = 1$ in the bottom row. The inset shows the projection $\mathcal{P}$ as a function of l for $\nu = 30$ for several b bands. Notice how much larger the drop in energy is between bands compared to the gaps between k states within a band.

lobe, which has a negligible impact on the overlap with the plane compared to the loss of pushing an entire set of lobes out of the plane. Within each m block, therefore, the diagonal elements will have large energy separations, and hence effectively decouple. The resulting states that share similar qualities are spread over many blocks and correspond to the series along the diagonal in Fig. 7. We label elements in these series with the values $b = 1, \ldots, \nu - 1$ and $k = 1, \ldots, \nu - b$. These numbers label the diagonals and the states in a given diagonal, respectively. Note that from the construction in Fig. 7 we have $l = 2b - 2 + m$ and $k = \nu - l$. The Fig. 7 inset displays the overlap $\mathcal{P}_{lm,lm}$ for various b as a function of l. Each b band smoothly changes with l, but the difference between b bands is large, especially so for the lowest b values.

The appearance of bands in the eigenspectrum (see Fig. 6) is essentially a consequence of the approximate b bands of similar states described in Fig. 7. The identity $b = \beta$ holds exactly when the m-block matrices are diagonal, i.e., in the asymptotic wings of these bands where the dispersion becomes approximately linear (see Fig. 6) and where $l \approx m \approx \nu$. Since in this limit the eigenenergies are obtained analytically and the real bands β coincide with the approximate bands b, we focus now on the behavior of these linear wings. If we consider only the diagonal matrix elements of Eq. (15),

$$\lim_{d\to 0} \tilde{V}_{lm,lm} = \frac{1}{\pi\nu^4}[N_{lm}P_l^m(0)]^2 R^{(1)}_{\nu l,\nu l} = \frac{1}{\pi\nu^4}\frac{2l+1}{2^{2l+1}\nu^2}\frac{(l-m)!(l+m)!}{[(\frac{l+m}{2})!(\frac{l-m}{2})!]^2}, \quad (16)$$

we obtain the energy levels for the ∼10 lowest energy levels in each band of states to a few percent accuracy, confirming that the diagonal approximation is appropriate. More importantly, by switching to the band numbers b and k, we can gain further intuition into the true bands, labeled by β, seen in Fig. 6. In the high ν limit we obtain the linear dispersion relation,

$$\tilde{E}^{2D}_{bk} \approx \frac{[8\nu + 4(b-k) - 1]\Gamma(b-1/2)}{8\pi^2\nu^{13/2}\Gamma(b)}. \quad (17)$$

In particular, band $b \approx \beta$ starts at the energy

$$\tilde{E}^{2D}_{b1} = \frac{\Gamma(b-1/2)}{\Gamma(b)}\frac{1}{\pi^2\nu^{11/2}}. \quad (18)$$

For $b \ll \nu$ the energies scale as $\nu^{-11/2}$. In particular, the lowest energy lies at $\tilde{E} = \nu^{-11/2}\pi^{-3/2}$. At higher b we use the limiting form of the Γ functions,

$$\lim_{b\to\infty} \frac{\Gamma(b-1/2)}{\Gamma(b)} = \frac{1}{\sqrt{b}}, \quad (19)$$

to obtain

$$\lim_{b\to\infty} \tilde{E}^{2D}_{bk} = \frac{1}{\pi^2\sqrt{b}\nu^{11}}. \quad (20)$$

The band's lower edges become more closely spaced in energy due to this $1/\sqrt{b}$ dependence. The level spacing within a band is given approximately by

$$\lim_{b\to\infty} \Delta_k = \frac{\Gamma(b-1/2)}{2\nu^{13/2}\pi^2\Gamma(b)} = \sqrt{\frac{1}{b}}\frac{1}{2\pi^2\nu^{13/2}}. \quad (21)$$

Taking this width as approximately constant over an entire band and taking the number of states per band to be $\sim\nu$, we find that the width of each band is approximately

$$\Delta \approx \frac{1}{2\pi^2}\frac{1}{\sqrt{b}\nu^{11/2}}. \quad (22)$$

On the other hand, the spacing between band minima is approximately

$$\Delta_b \approx \frac{d}{db}\frac{1}{\sqrt{b\nu^{11}}} \sim \frac{1}{\sqrt{b^3}\nu^{11/2}}. \quad (23)$$

Within this crude series of approximations we find that $(\Delta_b/\Delta) \propto (1/b)$. Because of this decreasing gap between bands relative to their own widths the bands begin to overlap, leading to the region of high-energy density seen in Figs. 2(b) and 5. As the bands overlap with increasing b, the expression for the band minimum, Eq. (18), tends toward ν^{-6}, since $b \sim \nu$. As the energy-level structure transitions from the "band" type into this denser structure of many overlapping bands, the functional form of the energy scaling changes from $\nu^{-11/2}$ to $\nu^{-12/2}$.

B. Scaling laws for scatterers in D dimensions

1. 2D scatterers

The preceding analysis showed that the energy spectrum of the 2D composite exhibits two different scaling behaviors as a function of band number. The energies in the lower bands scale as $\nu^{-5.5}$, but they scale as ν^{-6} in the upper bands due to a mixture of overlapping bands and deviations from the diagonal approximation for small values of l and m.

2. 1D scatterers

Applying this same analysis to our 1D and 3D configurations leads quickly to the result that all states experience an identical energy shift. In 1D, the expression equivalent to Eq. (12) is

$$\lim_{d\to 0}\tilde{V}_{lm,l'm'} = \frac{a_\nu}{V_1} 2\int_0^\infty \Phi^*_{\nu\times lm}(R,0,0)\Phi_{\nu l'm'}(R,0,0)dR$$
$$= \frac{a_\nu\sqrt{(2l+1)(2l'+1)}}{2\pi V_1} R^{(2)}_{\nu l,\nu l'}\,\delta_{m0}\delta_{m'0}. \quad (24)$$

Curiously, this radial matrix element vanishes when $l \neq l'$ [48]:

$$R^{(2)}_{nl,nl'} = \frac{1}{\nu^3(l+1/2)}\delta_{ll'}. \quad (25)$$

This leads to a simple expression for the energy shifts:

$$\lim_{d\to 0}\tilde{V}_{lm,l'm'} = \frac{a_\nu}{V_1\pi\nu^3}. \quad (26)$$

The Rydberg levels are identically affected by the scatterers and remain degenerate. Explicitly inserting the volume, we have

$$\tilde{E}^{1D}_{lm} = \frac{1}{2\pi\nu^5}. \quad (27)$$

The energies scale as ν^{-5}, decreasing slower with increasing ν than the 2D composite's energies.

3. 3D scatterers

For a homogeneous structure in 3D the matrix elements are even simpler:

$$\lim_{d\to 0}\tilde{V}_{lm,l'm'} = \frac{a_\nu^3}{V_3}\int_V \Phi^*_{\nu lm}(R,\theta,\varphi)\Phi_{\nu l'm'}(R,\theta,\varphi)d^3R. \quad (28)$$

This is the normalization integral, and thus all Rydberg states are again degenerate, but with a global shift,

$$\tilde{E}^{3D}_{lm} = \frac{3}{4\pi\nu^6}. \quad (29)$$

These scale as ν^{-6}. The Rydberg composite's spectrum thus obeys a power-law scaling behavior ν^f, where $f=-5$ in 1D, $f=-11/2$ in 2D, and $f=-6$ in 3D. Despite the fact that the monolayer gives an energy scaling intermediate between the other geometries, it leads to a nondegenerate, highly structured dense limit which is totally distinct from the 1D and 3D composites.

4. Interpolation of low and high band edge scaling for 2D scatterers

We now explore the DOS scaling in the 2D case in further detail to arrive at a universal DOS for 2D Rydberg composites in the homogeneous limit. We compute a smooth density of states,

$$\frac{\delta N}{\delta\tilde{E}} = \sum_{i=1}^{N} F(\tilde{E};\sigma,\widetilde{E}_i), \quad (30)$$

where F is a convolution function for the discrete data, i.e., a Gaussian or a box function centered at $\widetilde{E}_i$ and having width σ. We focus first on the "band" region, where the eigenfunctions are to a good approximation labeled by integers b and k, and which scale as $\nu^{-11/2}$. Since the number of states in the bands increases approximately linearly with ν, we rescale the widths also so that they decrease linearly in ν. Figure 8(a) shows the resulting DOS for three ν values using a Gaussian distribution for F. The agreement between different ν is excellent in this band region, breaking down as energy increases. In gray scale we overlay each band separately, showing how the total DOS is built up from these, and in particular how the overlapping

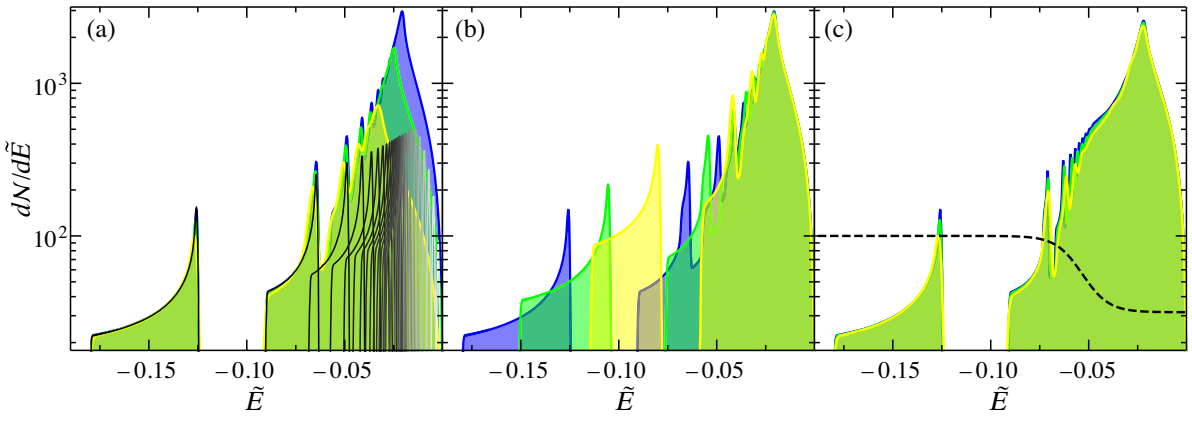

FIG. 8. Density of states computed by convolving the spectrum using a Gaussian distribution for three ν values: 40 (yellow), 70 (green), and 100 (blue). (a) The energies are scaled with $\nu^{5.5}$, the "band" scaling. Individual band contributions for $\nu=100$, obtained from the dispersion curves in Fig. 6, are shown in gray scale. (b) The energies are scaled with ν^6, the "overlap" scaling. (c) The energies and densities of states are scaled via the "universal" scaling connecting the band and overlap regions. The interpolating tanh function connecting the two regimes is overlayed. The FWHM of the convolving Gaussian distribution is approximately 0.0235; for details, see Appendix D.

bands create the saturation point in the DOS and the eventual onset of the ν^{-6} scaling law. Figure 8(b) shows a DOS with the ν^{-6} scaling, appropriate to the "overlap region" where the diagonal approximation breaks down. The widths now decrease as $\sigma/\sqrt{\nu}$ to obtain a smooth function. Some technical details involved in these figures are discussed in Appendix D.

Figure 8(c) presents a scaling that smoothly interpolates between these two regimes as a function of $\tilde{E}$. It allows us to construct a "universal" density of states for the 2D composite, independent of ν. Details of this process, which uses a hyperbolic tangent to map the relevant scale factors, widths, and normalizations between these two regions as a function of $\tilde{E}$, are provided in Appendix D. The DOS shown in Fig. 8(c) confirm that this scaling is indeed universal, as the DOS for the three different ν levels are essentially indistinguishable.

C. Spectrum of the spherical quantum dot composite

We return now to the SQD composite, introduced in Sec. II D, and study the spectrum of the 2D SQD composite in both the homogeneous limit and as a function of lattice spacing d. This illustrates the generic aspects of the Hamiltonian of Eq. (1) beyond the Rydberg composite, while also clarifying the presence and effects of the near separability of the Coulomb potential, which led to the bandlike structure exhibited by the 2D Rydberg composite. Since the SQD differs from the Rydberg system only in the radial wave functions and in the arrangement of nodal numbers within the degenerate manifold, we can rapidly adapt the preceding material to this system. For simplicity, we set the oscillator frequency to unity.

The matrix elements equivalent to Eq. (12) are

$$\lim_{d\to 0}\tilde{V}_{\mu lm,\mu l'm'} = \frac{\delta_{m,m'}}{\pi(2\mu+3)}\frac{2l+1}{2^{2l+1}}\frac{(l-m)!(l+m)!}{[(\frac{l+m}{2})!(\frac{l-m}{2})!]^2}\mathcal{R}^{(-1)}_{\mu l,\mu l'}, \quad (31)$$

which vanishes still when $l+m$ is odd since the spherical harmonics determine if there is a node at the monolayer. The radial matrix elements differ from those of Eq. (12), but are also analytically known [49]. As in the Rydberg composite, the resulting Hamiltonian is not diagonal. Nevertheless, upon numerical diagonalization we find that the eigenvalues are highly degenerate, as seen in Fig. 9. Rather than forming curving bands as a function of m like the Rydberg composite, they condense into flat bands as a function of m.

This implies that the system is exactly, rather than just approximately, separable. In the Rydberg composite, there were no additional degeneracies beyond the trivial one connecting states with equal $|m|$, since the Coulomb potential does not separate in any coordinate system compatible with the 2D lattice, i.e., Cartesian or cylindrical

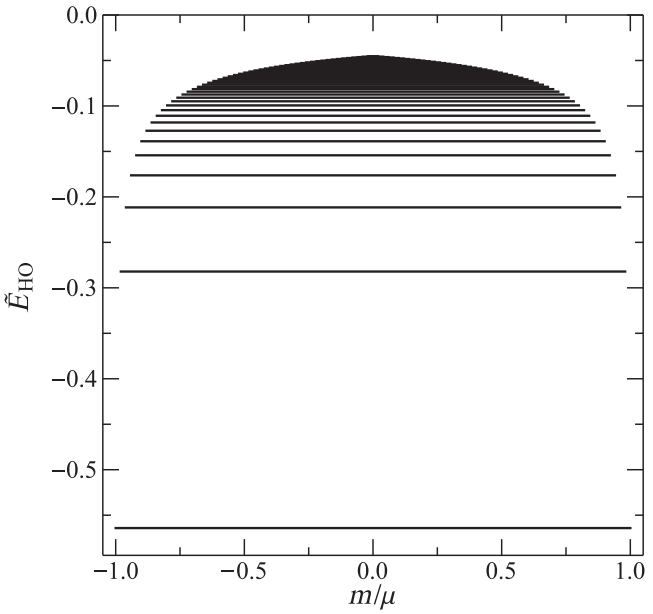

FIG. 9. The $\mu = 100$ eigenspectrum for a 2D SQD composite in the $d \to 0$ limit. The oscillator frequency is set to $\omega = 1$.

coordinates. For the SQD, however, we can write the harmonic potential as $V(\mathbf{r}) = \frac{1}{2}m\omega^2(x^2+y^2+z^2)$, compatible with the symmetry of the monolayer of scatterers in the $z=0$ plane. The matrix elements of the SQD composite's potential in Cartesian coordinates are easily obtained,

$$V_{n_x n_y n_z, n_x' n_y' n_z'} = \frac{\delta_{n_x,n_x'}\delta_{n_y,n_y'}\delta_{n_z,n_z'}}{\pi(2\nu+3)}|\Phi_{n_z}(0)|^2, \quad (32)$$

where $\Phi_{n_z}(z)$ is the standard one-dimensional hydrogen wave function. They are diagonal in the x, y nodal numbers due to the integration over the entire monolayer, and furthermore are diagonal in n_z, n_z' because of the constraint $\mu = n_x + n_y + n_z$. The resulting energy levels are simply

$$\tilde{E}_{\mathrm{HO}}(n_z) = \frac{1}{\pi(2\mu+3)}\frac{2^{n_z}\sqrt{\pi}}{n_z!(\Gamma[\frac{1-n_z}{2}])^2}. \quad (33)$$

The degeneracy of the n_zth level is $\mu - n_z + 1$, and the deepest shift $-\pi^{-1/2}$ is at $n_z = 0$. By comparing Fig. 6 with Fig. 9, it becomes clear how the band structure of the Rydberg composite emerges from the near separability of the monolayer potential. In the fully separable SQD case, the *degenerate* levels are determined by the single Cartesian nodal number n_z. Since no such quantity exists in the nonseparable Rydberg case, the energy levels, degenerate for the SQD, spread into bands, characterized by the band labels b and k.

We can see a similar phenomenon in the SQD case by going to lattice spacings d which are too big to result in a monolayer with homogenous scatterers to a homogenous monolayer—in such a case the separability is no longer

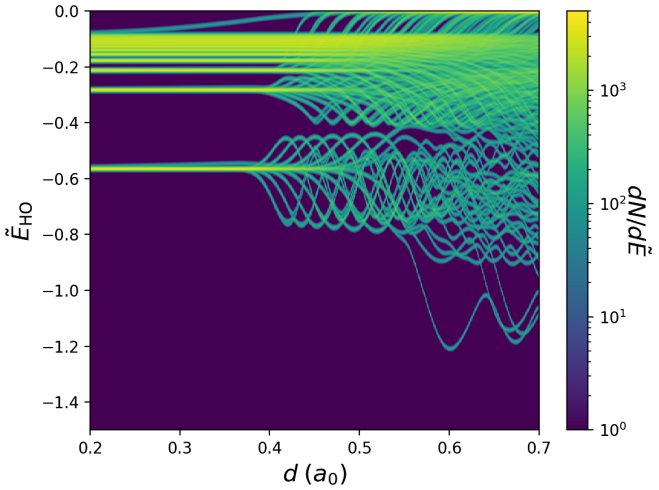

FIG. 10. Density of states for a $\mu = 30$ SQD composite as a function of lattice spacing d in atomic units. The oscillator frequency is set to $\omega = 1$ and the color is the same as in Fig. 2.

perfect. In Fig. 10 we show a density of states analogous to Fig. 2(b). This spectrum qualitatively resembles the 2D Rydberg composite spectrum at large lattice spacings, exhibiting all the real and avoided crossings, oscillating level shifts, and dense features visible there. At small spacings it shows a very similar limit as well, except with bands of essentially zero width compared to the large bands present in the Rydberg composite.

V. EVOLUTION OF THE SPECTRUM FOR DECREASING DENSITY OF SCATTERERS

We have thus investigated the nature of the spectrum in the limit where the lattice cannot be resolved by the Rydberg wave function. For the 2D composite this led to a nontrivial spectral density with bandlike structures, scaling laws, and Rydberg wave functions quite different from the ones known from atoms or molecules. In this section, we study the characteristics of this system at lattice spacings large enough to be resolved by the Rydberg wave function. To this end, we define a threshold lattice spacing d_c, below which the Rydberg wave function can no longer resolve the scatterers and which therefore replicates the homogeneous limit of scatterers, formally only reached for $d = 0$.

A. Transition to the homogeneous scatterer density

Several circumstances complicate a rigorous definition of d_c. First, the electron's wavelength varies spatially: in the radial direction it increases quadratically, while in the angular degree of freedom it is strongly l dependent. Second, since the potential depends nonlinearly on the wave function amplitude at the locations of the scatterers, it is not clear from the onset at what length scales scatterers can be resolved.

We have already seen that the homogeneous limit in the 2D case is heralded by wave functions which are diagonal in m. Near the bottom of each band these states are also approximately diagonal in l. Such a wave function has $2m$ angular nodes in the plane corresponding to an angular resolution π/m. The quadratic scaling of the radial nodes implies that their density decreases from the inner to the outer classical turning point. Therefore, the wave function can detect the smallest spatial features on a circle given by the inner classical turning point $R_{\min}$. The (angular) resolution corresponds to the distance separating two adjacent nodes on this circle, $w = R_{\min} \sin(\pi/m)$. Adapting w to a square lattice gives a critical lattice spacing equal to $w/\sqrt{2}$. Dropping terms of order ν^{-2} and assuming the angular resolution is smaller than any radial wave function feature, we arrive at a critical lattice spacing:

$$d_c(l,m) \approx \frac{\sin(\pi/m)\nu^2}{\sqrt{2}} \left[1 - \sqrt{1 - \frac{l(l+1)}{\nu^2}}\right]. \quad (34)$$

The black curves in Fig. 5 are lines through the points $(d_{\beta,m}, E_{\beta,m})$, where the connection between β and l is made with the approximate relation $l = 2(\beta - 1) - m$, as discussed in Sec. IV A. These fit well with the qualitative transitions seen in the spectrum for the lower bands where the approximations are more accurate. The transition can therefore be interpreted as the minimal spacing of scatterers which still can be resolved by the wave function. This spacing d_c should not be confused with d_D from Table I, which is the maximal spacing for breaking the degeneracy of all levels in the manifold ν. To keep the number of shifted states constant at $B_D = N_D$, considerations for the remainder of this section refer to $d \le d_D$ for $D = 2$ and $a = 2.5$.

B. Between the homogeneous and the few-scatterer limit: Chaotic spectra

Random matrix theory (RMT) is an appropriate framework to analyze chaotic spectra. Although the Rydberg composite's spectra are in principle chaotic, the application of RMT to the present problem is hindered by the fact that for $d > d_c$ the system obeys several symmetry constraints when $F = 1$. Moreover, toward the "trilobite limit" of only a few scatterers ($F \approx 0$ and or $d \gg d_c$), the spectrum becomes regular. Both properties strongly affect the mean density of states. Hence, standard tools [50] from RMT to describe properties of a classically chaotic system are cumbersome to implement as they require knowledge of the mean DOS for unfolding. The unfolded DOS has uniform mean density [51,52] and can be used to extract the eigenvalue correlations in the spectrum.

1. Adjacent gap ratio (AGR)

To avoid unfolding, we resort to the so-called adjacent gap ratio (AGR) [51,53],

$$\mathfrak{R} = \left\langle \frac{\min(s_n, s_{n-1})}{\max(s_n, s_{n-1})} \right\rangle, \tag{35}$$

with $s_n = E_n - E_{n-1}$ and the average $\langle\rangle$ taken over the whole spectrum. When $F \neq 1$, we also average over many lattice realizations. Since the AGR only depends on local fluctuations, it does not require unfolding [51]. The AGR can also deal with a "mixed" chaotic and regular spectrum, i.e., it can differentiate Poisson statistics, marking uncorrelated energies typically from preserved subspaces due to symmetries, from Gaussian orthogonal ensemble (GOE) statistics which occur for chaotic dynamics [50] without additional symmetries, when level repulsion is present [52]. The numerical AGR values corresponding to Poisson and GOE statistics are $\mathfrak{R}_P = 0.386$ and $\mathfrak{R}_{\mathrm{GOE}} = 0.530$, respectively. For further details, see Appendix E.

2. Evolution of AGR with the fill factor for different fixed lattice spacings

One can see in Fig. 11(a) that toward small fill factors, but compatible with $N > N_D$ where the spectrum looks chaotic, the AGR function $g_d(F)$ indeed approaches $g^0 \equiv \mathfrak{R}_{\mathrm{GOE}}$ for all d shown; see Appendix E. However, $g_d(F)$ breaks off g^0 for increasing F, to reach eventually the value $g_d(1) = 0$ due to geometry-induced degeneracy. For larger d, the breakoff occurs at larger F. For large d, the AGR function $g_d(F)$ approaches a boxlike shape with a sudden transition to $g_d(1) = 0$. We note here in passing that to a good approximation the family of functions $g_d(F)$ shown follow the form

$$[g_d(F)/g^0]^\gamma + F^\gamma = 1, \qquad \gamma = 1 + d/2, \tag{36}$$

an interesting relation revealing a self-similar property, whose deeper analysis is beyond the scope of this work.

3. Evolution of AGR for a filled lattice with decreasing lattice spacing

For a filled lattice $F = 1$, Fig. 11(b) reveals that neither GOE nor Poisson values match with the statistics observed for any lattice spacing d. For small d toward the homogeneous limit ($d_2 - d$ large), the AGR approaches zero again due to the geometrically induced degeneracies. However, for $d \to d_2$ in the chaotic regime the AGR settles to a value different from the GOE one due to the inherent symmetries of our system. We have simulated a chaotic system obeying the inherent "crystal" symmetries by a block-diagonal GOE matrix with each block representing one irreducible representation of the C_{4v} point group (see Appendix E). This synthetically obtained AGR [black line in Fig. 11(b)] agrees well with the AGR of the true spectrum for $d \to d_2$.

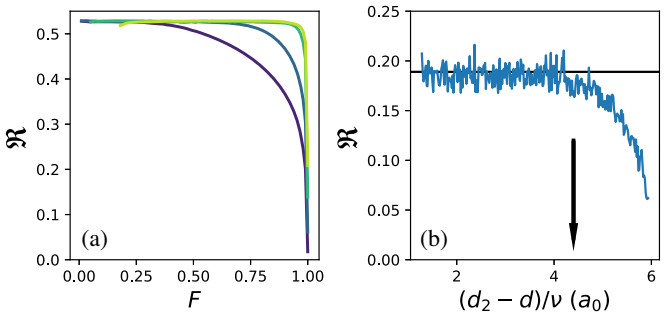

FIG. 11. (a) Average AGR of 2000 realizations of a lattice of scatterers as a function of F for $d = 5$, 10, 30, and 70 in sequence from dark to lighter line color, $\nu = 30$. (b) AGR for a filled lattice as a function of $(d_2 - d)/\nu$ with d_2 from d_D in Table I for $D = 2$. The arrow marks $d_c(l, m)$ from Eq. (34) with $m = l = \nu - 1$, while the horizontal line shows the RMT prediction for AGR incorporating the appropriate symmetries of the scatterers on the lattice; see text. Note that in both plots increasing values of the abscissa mean higher density of scatterers.

We may conclude that the spectral fluctuations in the DOS are indicative of a chaotic system with symmetries separating states into none interacting blocks in the $F = 1$ limit, while for $F \neq 1$ these symmetries gradually break until the spectrum is purely chaotic.

VI. EXPERIMENTAL REALIZATION

A. Isolation of Rydberg manifolds in the presence of scatterers

Rydberg composites live in the Hilbert space of a single Rydberg manifold ν. This implies that the excitation must be high enough such that interactions with adjacent manifolds is negligible. We have shown that the normalized energy levels of Rydberg composites in the dense lattice limit scale as ν^{-5}, $\nu^{-11/2}$, and ν^{-6} in 1D, 2D, and 3D, respectively. These energies must be compared, as a function of ν, with the overall spacing between Rydberg manifolds in order to ascertain the isolation of the Rydberg composite's manifold. In general, the coupling between energy levels increases inversely to their energetic separation, as can be seen with the Hellmann-Feynman theorem. Hence, we must confirm that the composite's spectrum does not overlap, or even approach, an adjacent Rydberg manifold. The spacing between Rydberg manifolds decreases as ν^{-3}, and hence the scaling of the unnormalized Rydberg composite's spectra must fall faster than this value. In 1D, the unnormalized spectrum is

$$E_1 \sim 2\pi |a_s| \tilde{V}_1 \frac{\nu^2}{d} \frac{1}{2\pi\nu^5} \propto \frac{|a_s|}{\nu^4}, \tag{37}$$

since $d \propto \nu$. In 2D, we have (for the strongest scaling, $\nu^{-11/2}$)

$$E_2 \sim 2\pi|a_s|\tilde{V}_2\frac{\nu^4}{d^2}\frac{1}{\pi^{3/2}\nu^{11/2}} \propto \frac{2|a_s|}{\sqrt{\pi}\nu^{7/2}}, \tag{38}$$

again, using $d \propto \nu$. Finally, in 3D, $d \propto \nu^{4/3}$, and so

$$E_3 \sim 2\pi|a_s|\tilde{V}_3\frac{\nu^6}{d^4}\frac{3}{4\pi\nu^6} \propto \frac{3}{2}\frac{|a_s|}{\nu^{16/3}}. \tag{39}$$

In all three cases the Rydberg composite's energies decrease faster than the splitting between manifolds as a function of ν, and hence at sufficiently high ν only the states of a single manifold contribute and the Rydberg composite exists as described.

B. Experimental choice of ν

Because of the scaling laws obtained in Sec. IV B, we have been able to focus our detailed numerical studies on rather moderate principal quantum numbers, $\nu \sim 30$, which are much simpler to calculate and analyze. However, we anticipate that both the true novelty of the Rydberg composite concept and the experimental study of its properties are aided by considering large ν values. From the conceptual side, as $\nu \to \infty$ a description of the system in terms of global features such as energy bands, level statistics, and scaling relations is more appropriate since the system becomes essentially continuous, possessing infinitely many levels. As the typical methods and perspectives of Rydberg atoms and molecules focus on the properties of individual states, the alternative scheme we have developed here clearly becomes essential at high ν. In addition to this conceptual reason, large ν values provide better justification for the various approximations we have employed, such as the use of a constant scattering length, neglect of interatomic potentials, neglect of higher partial wave scattering, restriction to a single ν manifold, etc. All of these approximations become more accurate at higher ν, but the rate at which they become valid as a function of ν can be accelerated by optimal choice of the atomic species. To ensure that the scatterer-shifted energy levels lie well between adjacent ν manifolds to prevent ν mixing, it might be desirable to choose a scatterer species with a smaller scattering length than Rb or Cs, the current standards. For example, sodium $(a_s(0) \sim -5)$and lithium $(a_s(0) \sim -7)$ have smaller scattering lengths than Rb $(a_s(0) \sim -16)$ [39]. The resonance energies of these atoms are also higher than in Rb or Cs, and hence p-wave scattering is even less relevant. Finally, as the next section shows, higher ν values are more favorable for the experimental construction of a Rydberg composite as they make it far easier to achieve the high particle number and increase the interatomic distances required to observe many of the key properties of the composite.

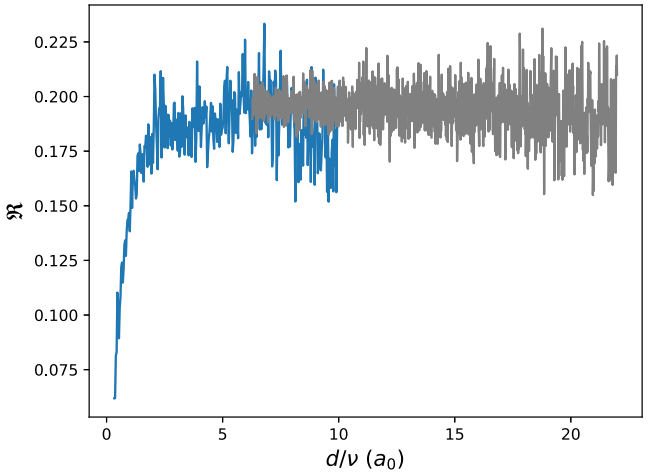

FIG. 12. Numerically obtained AGR for a Rydberg composite with $\nu = 30$ (blue) and $\nu = 100$ (gray) for a filled lattice ($F = 1$) as a function of d/ν.

C. Experimental construction of the Rydberg composite with scatterers on a lattice

The most serious obstacle to the creation of a Rydberg composite with a lattice of scatterers is probably the current experimental capability in creating small lattice spacings. If the experiment was performed in an optical lattice this would require quite a large principal quantum number, as the current minimum lattice spacing is around $d = \lambda/6 \sim 2500a_0$ [54]. A feature which should be possible to observe experimentally even at large lattice spacings is the onset of the chaotic behavior of the Rydberg composite's spectrum as discussed in Sec. V B. This chaotic behavior, heralded by the AGR value, is visible at large lattice spacings as seen in Fig. 12. The accessible d/ν values amenable to this AGR analysis increase with ν since more states are available, which reduces statistical fluctuations. Therefore, the AGR for $\nu = 100$ can be extended to well beyond $d/\nu = 10$ while the $\nu = 30$ AGR cannot. To reach an experimentally convenient range of lattice spacings one therefore benefits from larger Rydberg states, which is feasible given that Rydberg states with $\nu \sim 300$–500 have been produced [55–57].

D. Experimental realization of the Rydberg composite in a BEC

The interesting findings as we approach the homogeneous scatterer limit—in particular, features in the density of states such as its band structure and overall scaling behavior—do not require this lattice geometry, but only a large enough density of atoms within the Rydberg orbit. The critical constraint for an experimental realization is therefore simply that the atoms are densely spaced, but not necessarily in a regular pattern, rendering a lattice unnecessary. A random composite will have different energy level statistics (as seen in Sec. V), but, at least at high enough densities, the overall

features of the DOS will survive. To achieve the 2D composite and its characteristic band structure without an optical lattice, we rely on the possibility of strongly anisotropic trapping potentials which tightly confine the dense gas into a quasi-2D pancake shape. For sufficiently small width δz such a pancake geometry provides a physical realization of the 2D composite attainable with current experimental capabilities.

Sufficiently small in this context means that the Rydberg wave function cannot distinguish the quasi-2D scatterer geometry from the true 2D case. The out-of-plane resolving power is highest for the circular state $\nu = l + 1 = m + 1$. For large ν, $Y_{l=\nu,m=\nu}(\theta) \propto \exp[-\nu\theta^2/2]$ [58], and we take the standard deviation of this Gaussian to be the θ resolution of the state. Hence the resolving width is $\delta z \sim \nu^{3/2}$.

This means that for the pancake, as for the lattice, all of the Rydberg composite's properties scale favorably for an experimental realization with increasing ν. To provide an illustrative example we calculate the DOS of a pancake composite at a density $\sim 10^{15}$ cm^{-3}, which requires $\nu \approx 200$ and a pancake width $\delta z \approx 0.15$ μm. The density and thickness are both on the edge of what is immediately possible in experiments [59,60]. Of course, even larger ν [55–57] would increase the resolving width and allow the density to be decreased further.

Our calculations show [see Fig. 13(a)] that for the parameters specified, a band gap is indeed clearly visible. Since we have modeled the cloud after a realistic atomic vapor with nonuniform density, the density quoted ($\rho = 4 \times 10^{15}$ cm^{-3}) is the peak density at the center of the cloud. As the density increases the band gap gets sharper and deeper (not shown).

If the cloud is thicker there is no longer a band gap, but the band structure can still be observed, as shown in Fig. 13(b), where the thickness is $\delta_z = 0.3$ μm and the peak density $\rho = 8 \times 10^{15}$. Because of this higher thickness, the second band is no longer the $m = l - 2$, as is the case in the 2D composite, but instead the $m = l - 1$ band, as it is more tightly confined to the xy plane and thus experiences a larger overall energy shift once the atom cloud is thick enough to saturate the wave function's lobes that sit on either side of the plane. Figure 13 confirms that the gross features of the 2D composite studied here are observable under experimental conditions which can presently be attained.

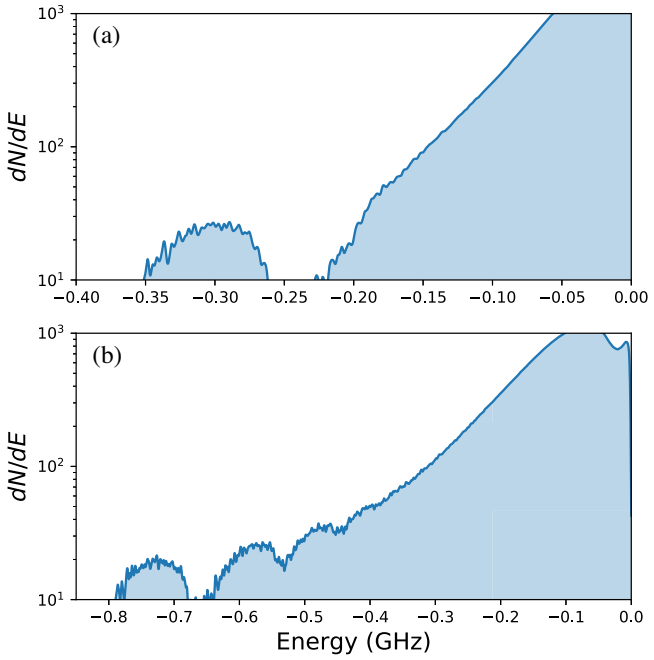

FIG. 13. The DOS for a $\nu = 200$ Rydberg composite formed with scatterers in a quasi-2D BEC in pancake geometry. The scatterers are randomly positioned with a uniform distribution in the xy plane and a Gaussian profile in the z direction. The cloud's peak density and width (standard deviation) in the z direction are, respectively, $\rho = 4 \times 10^{15}$ cm^{-3} and $\delta_z = 0.15$ μm in (a) and $\rho = 8 \times 10^{15}$ cm^{-3} and $\delta_z = 0.3$ μm in (b). We have convolved the line spectra with a Gaussian distribution of 1 MHz width and use the zero-energy electron-rubidium scattering length $a_s = -16.1 a_0$. The DOS is normalized by multiplying by a factor of $1/\nu$ as in Fig. 2(a).

E. Photoabsorption spectroscopy of the Rydberg composite

Of course, the DOS is not directly observable due to the selection rules governing laser excitation of the 2D composite. In the homogeneous limit these are quite strong due to the near separability of the system, and detection of

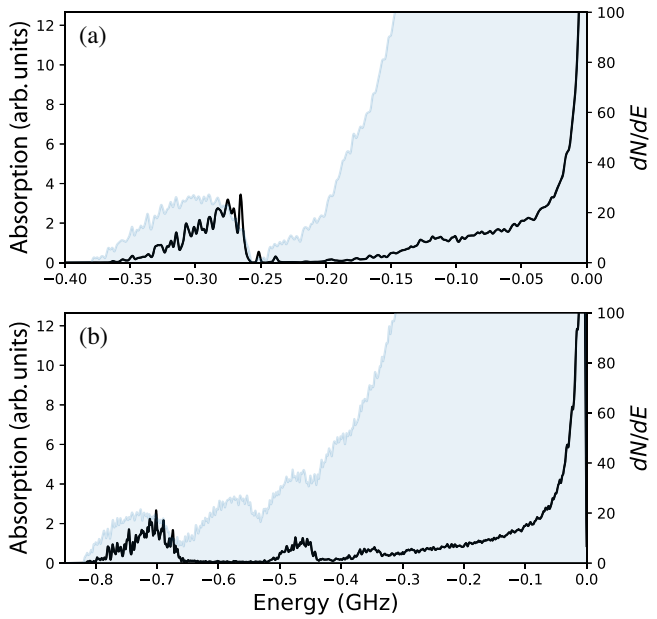

FIG. 14. Absorption spectra in arbitrary units from absorbing two circularly polarized photons (see text) for the pancake Rydberg composite of Fig. 13 (black line) and the corresponding DOS from Fig. 13 shown as blue shaded area. All parameters are as in Fig. 13.

the DOS would require either the breakdown of selection rules due to intense laser pulses or applied external fields or an alternative scheme altogether. In the case of the pancake BEC introduced above, the selection rules are not as strong and photoabsorption could indeed probe the DOS over a wide range of energies with nonzero oscillator strength. The available spectrum is therefore obtained by modulating the DOS with the transition strength to each state. As an example of what could be observed using a straightforward two-photon excitation scheme with circularly polarized light to access the $l = 2$, $m = 2$ component of the Rydberg composite states, we show in Fig. 14 exemplary spectra as black lines superimposed over the DOS from Fig. 13. The spectra feature similarly strong drops in strength at the band edges as the DOS and, particularly in the higher density example in Figs. 13(b) and 14(b), also show some of the band structure of the underlying DOS. The absorption spectrum of the latter is heavily suppressed in the second, fourth, etc., bands since they are formed from states dominated by odd $l - m$ values. The mixing of these states with $l = m - 2$ is negligible.

VII. CONCLUSIONS AND FUTURE WORK

In this article we introduced Rydberg composites built by coupling a Rydberg atom to a dense distribution of many neutral atoms immersed within the Rydberg wave function. Rydberg composites provide a systematic interpolation from the trilobite and polyatomic few-body regime to a dense environment with a homogeneous density of scatterers as the asymptotic limit. Rydberg composites, particularly the 2D monolayer case emphasized here, are a new form of matter intersecting few-body atomic Rydberg physics, quantum dynamics involving optical lattices, and few-body quasiparticle examples from solid-state physics.

One can imagine many immediate possibilities to extend this concept. These include more refined geometries of the embedding environment to tune the Rydberg composite spectrum, a goal which is traditionally reached by applying external electric or magnetic fields. Also, localization and decoherence studies are feasible by removing the frozen gas restriction and either shaking the lattice explicitly or allowing it to move randomly at some finite temperature.

Although the main focus of this work is on the Rydberg composite, we stress that many of the qualitative features and behavior exhibited here can be found generically in a variety of systems which could form composites. In Secs. II D and IV C we showed that a quantum dot realization of a composite based on a harmonic potential exhibits a similar spectrum. However, the energy bands characteristic for the Rydberg composite in the homogeneous limit of scatterers collapse for the spherical quantum dot composite to degenerate levels since the harmonic potential commutes with the homogenous 2D scatterer array. Any system which exhibits a spectrum of high degeneracy is in principle suitable as a building block for a composite when interfaced with scatterers.

Moreover, the Rydberg composite itself could materialize outside of an ultracold atomic vapor. One possibility is the solid-state domain, e.g., a Rydberg exciton in cuprous oxide or similar semiconductor materials. These excitons are directly analogous to hydrogenlike atomic states except for the screening of the Coulomb interaction by the material. This variance in the Rydberg constant between materials implies that, at a comparable ν to a Rydberg atom, the exciton is several orders of magnitude larger (exceeding the micrometer scale) than the Rydberg electronic wave function and has much smaller binding energies. Since these excitons exist in a lattice which could in principle be regularly doped by impurity atoms, they could be an excellent system to realize a Rydberg composite. However, fundamental questions must be addressed first due to the much lighter center of mass of the Rydberg exciton, the effect of the lattice symmetries and dopant materials on the initial unperturbed states, and detection possibilities. Another class of systems which could realize the very high density limit are excitations in nanodroplets, which contain many very closely spaced atoms in a small volume.

To summarize, Rydberg or more generally excitation composites define a class of quantum systems with highly degenerate eigenfunctions whose volume is large enough to encompass arrangements of scatterers, sizable in extension and number. They can break the degeneracy such that unusual energy spectra and properties of the composite emerge which can be tuned by the arrangement of the scatterers.

ACKNOWLEDGMENTS

We are grateful to an anonymous referee who raised the question of quantum dot composites. We acknowledge funding from the DFG Grants No. EI 872/4-1 and No. RO 1157/9-1 through the Priority program SPP 1929 (GiRyd). M. T. E. acknowledges support from an Alexander von Humboldt postdoctoral fellowship.

APPENDIX A: MATRIX REPRESENTATION IN THE "TRILOBITE BASIS"

In the context of polyatomic Rydberg molecules, it has previously proven useful to perform a change of basis from the manifold of Rydberg states $|\nu lm\rangle$ to the basis of trilobite *dimer* states $|i\rangle$ [61]. Each element of this nonorthogonal basis is a trilobite wave function extending from the Rydberg core to the ith scatterer:

$$\Upsilon(\mathbf{R}_i, \mathbf{r}) = \sum_{lm} \Phi^*_{\nu lm}(\mathbf{R}_i)\Phi_{\nu lm}(\mathbf{r}). \tag{A1}$$

This basis is ideal when $\nu^2 \gg M \gg 1$, as it greatly reduces the numerical challenges associated with the large

ν^2-dimensioned Rydberg basis. It furthermore provides significant qualitative insight into the structure and possible geometries of polyatomic molecules since the basis states give directly the contribution of each scatterer to the eigenstate. From this one can define alternative localization measures utilizing the information immediately available from these eigenvectors, or classify the states within this basis using the known symmetries of the scatterer configurations, as we do in Appendix C.

In this Appendix, we extend this method to the Rydberg composite. Since this system typically has $M \gg \nu^2$, the trilobite basis is no longer numerically beneficial. It can still provide useful qualitative insight, and in the infinite scatterer limit it leads to an alternative method, solving an integral equation, to obtain the spectrum.

Within our stated approximations, the representation of H in the trilobite basis is the $M \times M$ matrix $H_{ii'} = \Upsilon(\mathbf{R}_i, \mathbf{R}_{i'})$. One numerical advantage of this approach is that the matrix element $H_{ii'}$ can be expressed using only $u_{n0}(R)$ and $u'_{n0}(R)$, eliminating the need to evaluate many high-l wave functions when $\nu \gg 1$ [19]. If $M > B_D$, the diagonalization of $H_{ii'}$ in this representation yields $M - B_D$ vanishing eigenvalues in addition to the B_D shifted eigenvalues, and one numerical disadvantage lies in distinguishing these from real, but small, eigenvalues. As $M \to \infty$, the dimension of $H_{ii'}$ becomes infinite, and hence the eigenvalue equation becomes an integral equation,

$$\Psi(\mathbf{r}) = \frac{1}{\tilde{E}} \int_{\mathcal{V}} \Upsilon(\mathbf{R}, \mathbf{r}) \Psi(\mathbf{R}) d\mathcal{V}, \tag{A2}$$

where $\mathcal{V}$ is the scatterer volume in dimension D. Since $\Upsilon(\mathbf{R}, \mathbf{r})$ is separable, Eq. (A2) has solutions with eigenfunctions Ψ corresponding to eigenvalues $\tilde{E}$ when $\tilde{E}$ is obtained from the determinantal equation (in the matrix representation of Rydberg states):

$$0 = \det \left| \delta_{ll'} \delta_{mm'} - \frac{1}{\tilde{E}} \int_{\mathcal{V}} \Phi^*_{\nu lm}(\mathbf{R}) \Phi_{\nu l'm'}(\mathbf{R}) d\mathcal{V} \right|. \tag{A3}$$

This equation can be solved via a numerical root finder.

APPENDIX B: PARABOLIC COORDINATES

The hydrogen atom separates in many coordinate systems, and one should choose a coordinate system that is, if possible, adapted to the geometry of the scatterer distribution. For example, the eigenstate for a single scatterer is nearly proportional to a Rydberg basis wave function in ellipsoidal coordinates [62], and the scatterer operator in the dense lattice limit for 1D and 3D composites commutes with the Hamiltonian in spherical coordinates. In the 2D case, the spherical wave functions are clearly not well adapted to the scatterer distribution. Although cylindrical coordinates are well suited to the 2D composite's scatterer distribution, the Coulomb potential does not separate in these coordinates. It does, however, separate in parabolic coordinates:

$$x = \sqrt{\xi\eta} \cos\phi, \qquad y = \sqrt{\xi\eta} \sin\phi, \qquad z = \frac{1}{2}(\xi - \eta). \tag{B1}$$

These treat parabolas ξ and η on either side of the $z = 0$ plane democratically, and therefore could be more closely adapted to the 2D composite. As the following shows, the Hamiltonian in this coordinate system still must be numerically diagonalized, although it does have closed-form analytic matrix elements. We therefore present this calculation not for its direct usefulness to the problem at hand, but to define a potentially useful yet uncommonly employed starting point that could benefit future calculations of the properties of Rydberg composites.

The hydrogenic wave functions in these coordinates are

$$\begin{aligned}\Phi_{n_1,n_2,m}(\xi,\eta,\phi) = {} & \frac{e^{im\phi}}{\sqrt{n\pi}} e^{-(1/2)\beta(\eta+\xi)} (\eta\xi)^{|m|/2} \\ & \times (n_1 + |m|)!(n_2 + |m|)! L_{n_1}^{|m|}(\beta\xi) L_{n_2}^{|m|}(\beta\eta) \\ & \times \sqrt{\frac{n_1! n_2!}{[(n_1 + |m|)!(n_2 + |m|)!]^3}} \beta^{|m|+3},\end{aligned} \tag{B2}$$

where $\nu = n_1 + n_2 + |m| + 1$ and $\beta = (1/n)$. This is normalized with respect to the volume element, $(\xi + \eta)/4 d\xi d\eta d\phi$. The matrix elements of the scatterer potential are

$$\begin{aligned}V_{n_1 n_2 m, n_1' n_2' m'} = {} & 2 \int_0^\infty \int_0^\infty \int_0^{2\pi} \delta(\eta - \xi) \\ & \times \Phi_{n_1 n_2 m}(\xi,\eta,\varphi) \Phi_{n_1' n_2' m'}(\xi,\eta,\varphi) \\ & \times \frac{\xi + \eta}{4} d\eta d\xi d\varphi,\end{aligned} \tag{B3}$$

using

$$\delta(z) = \delta\left(\frac{1}{2}(\xi - \eta)\right) = 2\delta(\xi - \eta). \tag{B4}$$

Integration over φ again requires $m = m'$, while integration of ξ sets $\xi = \eta$. The resulting expression involves only an integral over η:

$$\begin{aligned}&\langle n_1 n_2 m | V | n_1' n_2' m' \rangle \\ &\quad = 2\pi \delta_{mm'} \int \eta \Phi_{n_1,n_2,m}(\eta,\eta,0) \Phi_{n_1' n_2' m'}(\eta,\eta,0) d\eta.\end{aligned} \tag{B5}$$

The allowed quantum numbers are also restricted such that $n_1 + n_2 = n_1' + n_2'$ since m is conserved. The general integral of this form has a closed-form solution,

$$\int_0^\infty e^{-2x/n}x^{2m+1}L_{n_1}^m(x/n)L_{n_2}^m(x/n)L_{n_1'}^m(x/n)L_{n_2'}^m(x/n)dx$$
$$=\frac{1}{(-1)^{4m}(n_1+m)!(n_2+m)!(n_1'+m)!(n_2'+m)!}$$
$$\times\sum_{i=m}^{n_1}\sum_{j=m}^{n_2}\sum_{k=m}^{n_1'}\sum_{l=m}^{n_2'}b_{in_1+m,m}b_{jn_2+m,m}b_{kn_1'+m,m}b_{ln_2'+m,m}\frac{(i+j+k+l+\kappa-4m)!\lambda^{i+j+k+l-4m}}{\alpha^{i+j+k+l+\kappa-4m+1}},\tag{B6}$$

where

$$b_{inm}^{\lambda}=\frac{\lambda^{i-m}(-1)^i(n!)^2}{(n-i)!(i-m)!i!},\tag{B7}$$

and $\kappa=2m+1$, $\alpha=2/(n_1+n_2+m+1)$, and $\lambda=\alpha/2$. Thus we obtain $(2m+1)\times(2m+1)$ block-diagonal matrices since n_1, n_2 are related to ν and m. Diagonalization of these matrices yields the spectrum computed in the text. Since the basis was not restricted to reject wave functions with no amplitude in the plane from the beginning, as we did in spherical coordinates, $\nu(\nu-1)/2$ of these eigenvalues vanish.

APPENDIX C: SYMMETRY-ADAPTED ORBITALS

In this Appendix, we briefly review the use of the projection operator method which, in conjunction with the trilobite basis representation developed in Appendix A, can be used to obtain the Rydberg composite's spectrum when the scatterer configuration is a member of a molecular point group. The particular utility of this approach is that it leads to a classification of the resulting degeneracies and level crossings in the spectrum in the finite lattice-size regime. The description here follows Ref. [19] and is valid only for the s-wave (contact potential) interactions used here; generalization to p-wave interactions requires additional complications [19]. We obtained the symmetry-adapted eigenstates via the following process: (i) Identify the relevant molecular point group. For example, the planar square lattice satisfies the C_{4v} molecular point group. (ii) Construct the labeled basis of trilobite functions $\mathbf{v}$, where $v_k=\Upsilon(\mathbf{R}_k,\mathbf{r})$. (iii) Every symmetry operator in the point group corresponds to a rotation or reflection matrix, denoted $\underline{r_i}$. This operator acts on the position vector $\mathbf{R}_k$ of each trilobite function in $\mathbf{v}$, changing it to a different position vector, i.e., $\underline{r_i}\mathbf{R}_k=\mathbf{R}_j$. (iv) With this information, define an operator $\mathcal{R}_i$ which acts not on the position vectors $\mathbf{R}_k$ but rather on the basis vector $\mathbf{v}$. Its elements are $(\mathcal{R}_i)_{jj'}=\delta_{jk}\delta_{j'k'}$, where k and k' are related by $\underline{r_i}\mathbf{R}_{k'}=\mathbf{R}_k$. (v) Equation 20 of Ref. [19], in conjunction with the point group's character table, yields the projection operators $\hat{\mathcal{P}}^j$. These are (when properly rank reduced) $(M_j\times M)$-dimensioned matrices, where $M_j=\mathrm{Tr}(\hat{\mathcal{P}}^j)$. These traces satisfy $\sum_j M_j=M$, and thus describe how the total number of eigenstates are partitioned into the irreducible representations. (vi) These projection operators are then used to partition the Hamiltonian $H_{ii'}$ into block-diagonal form, where each block $H_{kk'}^j$ is the reduced Hamiltonian for the jth irreducible representation. This is done via the transformation

$$H_{kk'}^j=\sum_{i=1}^M\sum_{i'=1}^M\mathcal{P}_{ki}^jH_{ii'}(\mathcal{P}^j)_{i'k'}^\dagger.\tag{C1}$$

Finally, each $H_{kk'}^j$ is diagonalized. The eigenstates of a given j exhibit avoided crossings when a parameter, such as d, changes, while the eigenstates corresponding to different irreducible representations (different j values) exhibit real crossings. To make this concrete, we see for the C_{4v} symmetry of the plane that exactly half (neglecting "round-off" errors due to the mismatch between lattice points in the square and the circular Rydberg orbit) of the eigenstates are in the 2D E irreducible representation, while the remaining 50% of the eigenstates are approximately evenly split among the remaining $A1$, $A2$, $B1$, and $B2$ irreducible representations.

APPENDIX D: FURTHER DETAILS ON THE SMOOTH DOS

This Appendix describes additional technical details regarding the density of states calculated in Sec. IV. We begin with the full expression for the density of states used to make Fig. 8.

$$\frac{\delta N}{\delta\tilde{E}}=\frac{1}{\nu^{1/g}b^2}\sum_{i=1}^{B_D}F\left(\tilde{E};\frac{\sigma b}{\nu^g},\tilde{E}_ib\nu^f\right).\tag{D1}$$

In this formula, $F(x;\sigma,x_i)$ is a function to convolve the discrete line spectra with a finite width distribution. In Fig. 8 a Gaussian function,

$$F(x;\sigma_G,x_G)=\frac{1}{\sqrt{2\pi\sigma_G^2}}e^{-(x-x_G)^2/2\sigma_G^2},\tag{D2}$$

was used. Other functions, e.g., box functions, could be chosen as well. As discussed in Sec. IV B 4, there are different scaling laws for the width σ_G and energy levels x_G for the different regions—"band" and "overlap"—of the

density of states. Specifically, in the band region this is handled by setting $f = 11/2$, $g = 1$, and $b = 1$. We found that $\sigma = 0.1$ sufficed to achieve the smooth resolution of Fig. 8(a). The integrated density of states is

$$N_{\text{band}} = \frac{B_D}{\nu}. \tag{D3}$$

In the overlap region we set $f = 6$ and $g = 1/2$; this rescaling of the widths is necessary since the overlap states are denser. The integrated DOS in this case is

$$N_{\text{overlap}} = \frac{B_D}{\nu^2 b^2}. \tag{D4}$$

One inelegant technical detail stems from the fact that the band and overlap regions span very different energy ranges due to the difference between the ν^6 and $\nu^{11/2}$ scale factors. As a result, we must apply a global compression of the overlap energies by multiplying by a somewhat arbitrary factor, b, and afterward normalize the amplitude of the overall expression with a factor b^{-2}. We find that $b = 0.1$ sets, for this range of ν, the two scaled DOS to lie between the same ordinate and abscissa limits.

The fully universal scaling of the whole DOS is accomplished by making b, f, and g functions of $\tilde{E}$:

$$\frac{\delta N}{\delta \tilde{E}} = \frac{1}{\nu^{1/g(\tilde{E})} b(\tilde{E})^2} \sum_{i=1}^{N} F\left(\tilde{E}; \frac{\sigma b(\tilde{E})}{\nu^{g(\tilde{E})}}, \widetilde{E}_i b(\tilde{E}) \nu^{f(\tilde{E})}\right). \tag{D5}$$

For each of these fit functions we have found that a tanh function is sufficient to interpolate between band and overlap regions. Spanning the range from v_1 to v_2 with a width w and center x_0 provides a smooth interpolating function to transition between these two regions once these parameters are fit to the data.

$$f(x) = v_1 + \frac{v_2 - v_1}{2}\left[1 + \tanh\left(\frac{x - x_0}{w}\right)\right]. \tag{D6}$$

For the case shown in Fig. 8, $x_0 = -0.011$ and $w = 0.0028$.

APPENDIX E: AGR

The random matrix AGR values were all calculated by diagonalizing 2000 realizations of real symmetric matrices whose matrix elements were randomly sampled from a normal distribution. The AGR values have a weak dependence on matrix size.

The AGR value for the GOE case was found to be $\mathfrak{R}_{\text{GOE}} = 0.5304 \pm 0.0003$ using dense random matrices. The Poisson value was found to be $\mathfrak{R}_P = 0.3864 \pm 0.0003$ using a random matrix with elements only down the diagonal. These values were calculated on matrices of size 465×465, corresponding to B_2 for the $\nu = 30$ 2D composite.

In the case of $F \approx 1$, the symmetries of the system need to be taken into account. There are two limiting cases, the homogeneous and large d case. The AGR value in the homogeneous case is trivially zero since each eigenenergy is doubly degenerate due to the $\pm m$ symmetry. The system in the large d case belongs to the C_{4v} symmetry group. The C_{4v} character table has five different types of irreducible representation in it and only states in the same irreducible representation can interact with one another. One of the irreducible representations is two dimensional, meaning that each state belonging to it is doubly degenerate.

The AGR value for the large d case is calculated using matrices constructed of six GOE matrices in a block-diagonal format. The size of each block is chosen to match the number of states in each symmetry irreducible representation found in Appendix C. Four of the blocks are of size 56 (to account for the one-dimensional irreducible representations) while the last two are identical (to account for the two-dimensional irreducible representation) and of size 120 each. From this we obtain a value of $\mathfrak{R}_{d_{\text{large}}} = 0.1894 \pm 0.0002$.

In the homogeneous limit the AGR value is exactly zero due to the (trivial) degeneracy in m. The latter can be removed, either by ignoring every second state or only including states with positive m in the basis. Calculating the AGR for the remaining states produces $\mathfrak{R}_{m\geq 0} = 0.5279$ for $\nu = 30$, which is in good agreement with the $\mathfrak{R}_{\text{GOE}}$ value. The small difference can partially be attributed the band gap in the DOS.

APPENDIX F: RANK OF THE POTENTIAL MATRIX

To determine the rank of the potential matrix Eq. (4), we note that its form implies that every additional zero-range potential from a new scatterer shifts one more state out of the degenerate Rydberg manifold until the number of scatterers exceeds the size of the degenerate manifold. Hence, we can rewrite Eq. (4) as a sum over separable matrices,

$$V_{lm,l'm'} = 2\pi a_s \sum_{i}^{N_D} \phi_i \phi_i^{\dagger}, \tag{F1}$$

where $\phi_i = \{\phi_{\nu lm}(\mathbf{R}_i)\}$ is a vector of the degenerate hydrogen wave functions evaluated at the position of the ith scatterer. Since each term of this sum has rank 1, the total matrix has rank N_D. Therefore, each additional scatterer splits away an additional nonzero eigenstate, provided the vector ϕ_i is nonzero and linearly independent of the previous ϕ_i. Once $N_D > B_D$, additional scatterers have no effect on the number of nonzero states as the rank of the matrix is limited by the dimension B_D of the subspace interacting with scatterers.

[1] C. H. Greene, A. S. Dickinson, and H. R. Sadeghpour, *Creation of Polar and Nonpolar Ultra-Long-Range Rydberg Molecules*, Phys. Rev. Lett. **85**, 2458 (2000).

[2] I. C. H. Liu and J. M. Rost, *Polyatomic Molecules Formed with a Rydberg Atom in an Ultracold Environment*, Eur. Phys. J. D **40**, 65 (2006).

[3] I. C. H. Liu, J. Stanojevic, and J. M. Rost, *Ultra-Long-Range Rydberg Trimers with a Repulsive Two-Body Interaction*, Phys. Rev. Lett. **102**, 173001 (2009).

[4] V. Bendkowsky, B. Butscher, J. Nipper, J. P. Shaffer, R. Löw, and T. Pfau, *Observation of Ultralong-Range Rydberg Molecules*, Nature (London) **458**, 1005 (2009).

[5] V. Bendkowsky, B. Butscher, J. Nipper, J. B. Balewski, J. P. Shaffer, R. Löw, T. Pfau, W. Li, J. Stanojevic, T. Pohl, and J. M. Rost, *Rydberg Trimers and Excited Dimers Bound by Internal Quantum Reflection*, Phys. Rev. Lett. **105**, 163201 (2010).

[6] S. T. Rittenhouse, M. Mayle, P. Schmelcher, and H. R. Sadeghpour, *Ultralong-Range Polyatomic Rydberg Molecules Formed by a Polar Perturber*, J. Phys. B **44**, 184005 (2011).

[7] S. T. Rittenhouse and H. R. Sadeghpour, *Ultracold Giant Polyatomic Rydberg Molecules: Coherent Control of Molecular Orientation*, Phys. Rev. Lett. **104**, 243002 (2010).

[8] J. Aguilera-Fernández, H. R. Sadeghpour, P. Schmelcher, and R. González-Férez, *Electronic Structure of Ultralong-Range Rydberg Penta-atomic Molecules with Two Polar Diatomic Molecules*, Phys. Rev. A **96**, 052509 (2017).

[9] M. Mayle, S. T. Rittenhouse, P. Schmelcher, and H. R. Sadeghpour, *Electric Field Control in Ultralong-Range Triatomic Polar Rydberg Molecules*, Phys. Rev. A **85**, 052511 (2012).

[10] T. Kazimierczuk, D. Fröhlich, S. Scheel, H. Stolz, and M. Bayer, *Giant Rydberg Excitons in the Copper Oxide* Cu_2O, Nature (London) **514**, 343 (2014).

[11] P. Schauß, M. Cheneau, M. Endres, T. Fukuhara, S. Hild, A. Omran, T. Pohl, C. Gross, S. Kuhr, and I. Bloch, *Observation of Spatially Ordered Structures in a Two-Dimensional Rydberg Gas*, Nature (London) **491**, 87 (2012).

[12] C. Ates, T. Pohl, T. Pattard, and J. M. Rost, *Many-Body Theory of Excitation Dynamics in an Ultracold Rydberg Gas*, Phys. Rev. A **76**, 013413 (2007).

[13] G. Pupillo, A. Micheli, M. Boninsegni, I. Lesanovsky, and P. Zoller, *Strongly Correlated Gases of Rydberg-Dressed Atoms: Quantum and Classical Dynamics*, Phys. Rev. Lett. **104**, 223002 (2010).

[14] R. Schmidt, J. D. Whalen, R. Ding, F. Camargo, G. Woehl, S. Yoshida, J. Burgdörfer, F. B. Dunning, E. Demler, H. R. Sadeghpour, and T. C. Killian, *Theory of Excitation of Rydberg Polarons in an Atomic Quantum Gas*, Phys. Rev. A **97**, 022707 (2018).

[15] F. Camargo, R. Schmidt, J. D. Whalen, R. Ding, G. Woehl, S. Yoshida, J. Burgdörfer, F. B. Dunning, H. R. Sadeghpour, E. Demler, and T. C. Killian, *Creation of Rydberg Polarons in a Bose Gas*, Phys. Rev. Lett. **120**, 083401 (2018).

[16] A. Gaj, A. T. Krupp, J. B. Balewski, R. Löw, S. Hofferberth, and T. Pfau, *From Molecular Spectra to a Density Shift in Dense Rydberg Gases*, Nat. Commun. **5**, 4546 (2014).

[17] R. Schmidt, H. R. Sadeghpour, and E. Demler, *Mesoscopic Rydberg Impurity in an Atomic Quantum Gas*, Phys. Rev. Lett. **116**, 105302 (2016).

[18] P. J. J. Luukko and J. M. Rost, *Polyatomic Trilobite Rydberg Molecules in a Dense Random Gas*, Phys. Rev. Lett. **119**, 203001 (2017).

[19] M. T. Eiles, J. Pérez-Ríos, F. Robicheaux, and C. H. Greene, *Ultracold Molecular Rydberg Physics in a High Density Environment*, J. Phys. B **49**, 114005 (2016).

[20] I. Bloch, *Ultracold Quantum Gases in Optical Lattices*, Nat. Phys. **1**, 23 (2005).

[21] S. Hollerith, J. Zeiher, J. Rui, A. Rubio-Abadal, V. Walther, T. Pohl, D. M. Stamper-Kurn, I. Bloch, and C. Gross, *Quantum Gas Microscopy of Rydberg Macrodimers*, Science **364**, 664 (2019).

[22] S. de Léséleuc, V. Lienhard, P. Scholl, D. Barredo, S. Weber, N. Lang, H. P. Büchler, T. Lahaye, and A. Browaeys, *Observation of a Symmetry-Protected Topological Phase of Interacting Bosons with Rydberg Atoms*, Science **365**, 775 (2019).

[23] D. Ohl de Mello, D. Schäffner, J. Werkmann, T. Preuschoff, L. Kohfahl, M. Schlosser, and G. Birkl, *Defect-Free Assembly of 2D Clusters of More Than 100 Single-Atom Quantum Systems*, Phys. Rev. Lett. **122**, 203601 (2019).

[24] H. Bernien, S. Schwartz, A. Keesling, H. Levine, A. Omran, H. Pichler, S. Choi, A. S. Zibrov, M. Endres, M. Greiner *et al.*, *Probing Many-Body Dynamics on a 51-Atom Quantum Simulator*, Nature (London) **551**, 579 (2017).

[25] D. Rychtarik, B. Engeser, H.-C. Nägerl, and R. Grimm, *Two-Dimensional Bose-Einstein Condensate in an Optical Surface Trap*, Phys. Rev. Lett. **92**, 173003 (2004).

[26] N. L. Smith, W. H. Heathcote, G. Hechenblaikner, E. Nugent, and C. J. Foot, *Quasi-2D Confinement of a BEC in a Combined Optical and Magnetic Potential*, J. Phys. B **38**, 223 (2005).

[27] I. Bloch, J. Dalibard, and W. Zwerger, *Many-Body Physics with Ultracold Gases*, Rev. Mod. Phys. **80**, 885 (2008).

[28] Z. Hadzibabic, P. Krüger, M. Cheneau, B. Battelier, and J. Dalibard, *Berezinskii–Kosterlitz–Thouless Crossover in a Trapped Atomic Gas*, Nature (London) **441**, 1118 (2006).

[29] J. Keski-Rahkonen, P. J. J. Luukko, L. Kaplan, E. J. Heller, and E. Räsänen, *Controllable Quantum Scars in Semiconductor Quantum Dots*, Phys. Rev. B **96**, 094204 (2017).

[30] J. Keski-Rahkonen, P. J. J. Luukko, S. Åberg, and E. Räsänen, *Effects of Scarring on Quantum Chaos in Disordered Quantum Wells*, J. Phys. Condens. Matter **31**, 105301 (2019).

[31] C. C. Liu, T. H. Lu, Y. F. Chen, and K. F. Huang, *Wave Functions with Localizations on Classical Periodic Orbits in Weakly Perturbed Quantum Billiards*, Phys. Rev. E **74**, 046214 (2006).

[32] A. Sitenko and O. Gerasimov, *Elastic Electron Scattering from a Multicentred Potential*, Phys. Lett. A **171**, 71 (1992).

[33] A. Baltenkov, *The Application of General Zero-Range Potentials to Multi-Center Problems*, Phys. Lett. A **268**, 92 (2000).

[34] E. Demiralp, *Bound States of n-Dimensional Harmonic Oscillator Decorated with Dirac Delta Functions*, J. Phys. A **38**, 4783 (2005).

[35] H. Uncu, D. Tarhan, E. Demiralp, and Ö. E. Müstecaplıoğlu, *Bose-Einstein Condensate in a Harmonic Trap Decorated with Dirac δ Functions*, Phys. Rev. A **76**, 013618 (2007).

[36] E. Fermi, *Pressure Broadening of High-Lying Spectral Lines*, Il Nuovo Cimento **11**, 157 (1934).

[37] C. Bahrim and U. Thumm, *Low-Lying $^3P^o$ and $^3S^e$ States of Rb^-, Cs^-, and Fr^-*, Phys. Rev. A **61**, 022722 (2000).

[38] A. Omont, *On the Theory of Collisions of Atoms in Rydberg States with Neutral Particles*, J. Phys. (Paris) **38**, 1343 (1977).

[39] M. T. Eiles, *Formation of Long-Range Rydberg Molecules in Two-Component Ultracold Gases*, Phys. Rev. A **98**, 042706 (2018).

[40] C. Fey, M. Kurz, P. Schmelcher, S. T. Rittenhouse, and H. R. Sadeghpour, *A Comparative Analysis of Binding in Ultralong-Range Rydberg Molecules*, New J. Phys. **17**, 055010 (2015).

[41] D. A. Anderson, S. A. Miller, and G. Raithel, *Angular-Momentum Couplings in Long-Range* Rb_2 *Rydberg Molecules*, Phys. Rev. A **90**, 062518 (2014).

[42] M. T. Eiles and C. H. Greene, *Hamiltonian for the Inclusion of Spin Effects in Long-Range Rydberg Molecules*, Phys. Rev. A **95**, 042515 (2017).

[43] F. Hummel, C. Fey, and P. Schmelcher, *Spin-Interaction Effects for Ultralong-Range Rydberg Molecules in a Magnetic Field*, Phys. Rev. A **97**, 043422 (2018).

[44] Y. Ashida, T. Shi, R. Schmidt, H. R. Sadeghpour, J. I. Cirac, and E. Demler, *Quantum Rydberg Central Spin Model*, Phys. Rev. Lett. **123**, 183001 (2019).

[45] E. Amaldi and E. Segrè, *Effect of Pressure on High Terms of Alkaline Spectra*, Nature (London) **133**, 141 (1934).

[46] C. Füchtbauer and F. Gössler, *Shift and Asymmetric Broadening of Absorption Lines through Gaseous Contaminants*, Z. Phys. **87**, 89 (1934).

[47] C. Fey, F. Hummel, and P. Schmelcher, *Building Principle of Triatomic Trilobite Rydberg Molecules*, Phys. Rev. A **99**, 022506 (2019).

[48] M. Enciso-Aguilar, J. López-Bonilla, and M. Sánchez-Meraz, *Radial Matrix Elements for the Hydrogen Atom*, Electron. J. Theor. Phys. **13**, 117 (2006), http://www.ejtp.com/articles/ejtpv3i13p117.pdf.

[49] C. Chang-Yuan, *General Formula and Recurrence Formula for Radial Matrix Elements of N-Dimensional Isotropic Harmonic Oscillator*, Chin. Phys. **9**, 731 (2000).

[50] M. C. Gutzwiller, *Chaos in Classical and Quantum Mechanics* (Springer Science & Business Media, Berlin, 1990), Vol. 1.

[51] Y. Y. Atas, E. Bogomolny, O. Giraud, and G. Roux, *Distribution of the Ratio of Consecutive Level Spacings in Random Matrix Ensembles*, Phys. Rev. Lett. **110**, 084101 (2013).

[52] F. Haake, *Random-Matrix Theory*, in *Quantum Signatures of Chaos* (Springer, Berlin, 2001), pp. 47–118.

[53] V. Oganesyan and D. A. Huse, *Localization of Interacting Fermions at High Temperature*, Phys. Rev. B **75**, 155111 (2007).

[54] R. P. Anderson, D. Trypogeorgos, A. Valdés-Curiel, Q.-Y. Liang, J. Tao, M. Zhao, T. Andrijauskas, G. Juzeliūnas, and I. B. Spielman, *Realization of a Deeply Subwavelength Adiabatic Optical Lattice*, Phys. Rev. Research **2**, 013149 (2020).

[55] S. Ye, X. Zhang, T. C. Killian, F. B. Dunning, M. Hiller, S. Yoshida, S. Nagele, and J. Burgdörfer, *Production of Very-High-n Strontium Rydberg Atoms*, Phys. Rev. A **88**, 043430 (2013).

[56] M. T. Frey, S. B. Hill, K. A. Smith, F. B. Dunning, and I. I. Fabrikant, *Studies of Electron-Molecule Scattering at Microelectronvolt Energies Using Very-High-n Rydberg Atoms*, AIP Conf. Proc. **360**, 815 (1996).

[57] M. T. Frey, F. B. Dunning, C. O. Reinhold, and J. Burgdörfer, *Ionization of Very-High-n Rydberg Atoms by Half-Cycle Pulses in the Short-Pulse Regime*, Phys. Rev. A **53**, R2929 (1996).

[58] I. Barth and C. Lasser, *Trigonometric Pulse Envelopes for Laser-Induced Quantum Dynamics*, J. Phys. B **42**, 235101 (2009).

[59] D. M. Stamper-Kurn, M. R. Andrews, A. P. Chikkatur, S. Inouye, H.-J. Miesner, J. Stenger, and W. Ketterle, *Optical Confinement of a Bose-Einstein Condensate*, Phys. Rev. Lett. **80**, 2027 (1998).

[60] R. Saint-Jalm, P. C. M. Castilho, E. Le Cerf, B. Bakkali-Hassani, J.-L. Ville, S. Nascimbene, J. Beugnon, and J. Dalibard, *Dynamical Symmetry and Breathers in a Two-Dimensional Bose Gas*, Phys. Rev. X **9**, 021035 (2019).

[61] M. T. Eiles, *Trilobites, Butterflies, and Other Exotic Specimens of Long-Range Rydberg Molecules*, J. Phys. B **52**, 113001 (2019).

[62] B. E. Granger, E. L. Hamilton, and C. H. Greene, *Quantum and Semiclassical Analysis of Long-Range Rydberg Molecules*, Phys. Rev. A **64**, 042508 (2001).